SAND2021-3574J

Detecting and Imaging Stress Corrosion Cracking in Stainless Steel, with Application to Inspecting Storage Canisters for Spent Nuclear Fuel

Marcel C. Remillieux,[1] Djamel Kaoumi,[2] Yoshikazu Ohara,[3] Marcie A. Stuber Geesey,[1] Li Xi,[2] Ryan Schoell,[2] Charles R. Bryan,[4] David G. Enos,[4] Deborah A. Summa,[5] T. J. Ulrich,[6] Brian E. Anderson,[7] Zeev Shayer.[8]

[1]Geophysics Group (EES-17), Los Alamos National Laboratory, Los Alamos, NM, USA
[2]Department of Nuclear Engineering, North Carolina State University, NC, USA
[3]Department of Materials Processing, Tohoku University, Sendai 980-8579, Japan
[4]Sandia National Laboratories, Albuquerque, NM, USA
[5]Non-Destructive Testing and Evaluation Group (E-6), Los Alamos National Laboratory, Los Alamos, NM, USA
[6]Detonation Science and Technology (Q-6), Los Alamos National Laboratory, Los Alamos, NM, USA
[7]Department of Physics and Astronomy, Brigham Young University, Provo, UT 84602, USA
[8]Department of Physics, Colorado School of Mines, Golden, CO, USA

Abstract

One of the primary concerns with the long-term performance of storage systems for spent nuclear fuel (SNF) is the potential for corrosion initiation due to deliquescence of salts deposited as aerosols on the surface of the canister, which is typically made of austentic stainless steel. In regions of high residual weld stresses, this may lead to localized stress-corrosion cracking (SCC). The ability to detect and image SCC at an early stage (long before the cracks are susceptible to propagate through the thickness of the canister wall and leaks of radioactive material may occur) is essential to the performance evaluation and licensing process of the storage systems. In this paper, we explore a number of nondestructive testing techniques to detect and image SCC in austenitic stainless steel. Our attention is focused on a small rectangular sample of 1×2 in^2 with two cracks of mm-scale sizes. The techniques explored in this paper include nonlinear resonant ultrasound spectroscopy (NRUS) for detection, Linear Elastodynamic Gradient Imaging Technique (LEGIT), ultrasonic C-scan, vibrothermography, and synchrotron X-ray diffraction for

Sandia National Laboratories is a multimission laboratory managed and operated by National Technology & Engineering Solutions of Sandia, LLC, a wholly owned subsidiary of Honeywell International Inc., for the U.S. Department of Energy's National Nuclear Security Administration under contract DE-NA0003525.

imaging. Results obtained from these techniques are compared. Cracks of mm-scale sizes can be detected and imaged with all the techniques explored in this study.

1. Introduction

Currently Spent Nuclear Fuel (SNF) is stored in two types of environmental storage conditions; 1) submerged in water in pools at reactor facilities, and 2) in dry storage at Independent Spent Fuel Storage Installations (ISFSIs), adjacent to reactor facilities. Generally after a few years of cooling time, SNF is removed from the water pool and transferred to helium-filled stainless steel canisters and stored in a passively ventilated concrete overpack, which acts as a dry storage systems. As a result of several recent decisions, such as not pursuing Yucca Mountain as a long-term geologic repository storage facility for SNF and the cancellation of the construction of a reprocessing facility in the 1980s due to proliferation risks, interim dry storage facilities for long-term storage are vital for the immediate future of nuclear energy technology. One of the primary concerns with respect to the long-term performance of the storage casks is the potential for corrosion initiation due to deliquescence of salts deposited on the canister surface as aerosols. In regions of high residual weld stresses, this may lead to localized stress corrosion cracking (SCC). Dust and aerosols in the air being drawn though ventilation openings in the concrete overpack may be deposited on the stainless steel canister outer surfaces. Under these conditions, localized corrosion may occur. Chloride-induced stress corrosion cracking (CISCC) of welded heat affected zones (HAZ) is of special concern, as it is a well-documented mode of attack for austenitic stainless steels (including 304H/L and 316L) in marine environments [1], and many ISFSI sites are located in coastal areas. Recent canister inspections [2,3] have shown that chloride salts are present on the surface of in-service canisters in near-marine sites.

For a number of safety reasons, it is strongly preferred to leave the canister inside the concrete overpack once installed there. This makes the inspection of canister surfaces very challenging, mainly because of the harsh environment and space constraints. The inspection system should be designed to sustain high temperatures (typically 205°C upon loading the canister into the overpack down to less than 150°C after 30 years) and gamma radiation (in the range of 10^3 to 10^5 rad/h) [4]. The space constraints include restricted access through the narrow ventilation system and narrow rectangular channels between the overpack and the canister. On the HI-STORM 100 model cask

(Holtec International, Turtle Creek, PA, USA), these channels have dimensions of 50 mm by 150 mm [4]. All the welds and associated HAZs cannot be visible or accessible from all the channels, thus leaving some blind spots that cannot be inspected with visual techniques. Some recent work from the group of Lissenden at Pennsylvania State University has shown the possibility to access and inspect this tight space with robots instrumented with EMAT acoustic sensors [5,6]. The detection technique they used is based on the acoustic echoes generated by defects along the propagation path of the wave. They demonstrated their approach on a sample that had a notch in the HAZ to simulate the presence of a crack. The notch could be detected but so could the reflection from the back wall, the weld, and other reflectors. Similar limitations would be encountered with any technique based on linear acoustics or linear wave propagation, including C-scans, eddy currents, or angle-beam ultrasound. Furthermore, in the early stage of damage or under certain stress conditions, the crack may be present but not necessarily open, in which case no reflection of the incident acoustic wave would be produced, thus possibly making the crack invisible to these techniques.

This paper focuses on a number of techniques based on acoustics and/or optics that adapted to the detection and imaging of cracks at an early stage of damage. To this end, a sample with small cracks (less than 2 mm in length) is used throughout the study. Some of the crack detection techniques, such as ultrasonic C-scan, are well established in the field [7], while others, such as Linear Elastodynamic Gradient Imaging Technique (LEGIT), have been developed in-house. Each crack-detection technique is introduced briefly here, since additional background information is provided in the individual sections for each technique. Last, detailed 3D images of the cracks are created using synchrotron X-ray diffraction, which is used only as a reference here without any objective of field deployment.

The first technique discussed is ultrasonic C-scan, which relies on linear ultrasonics. When an ultrasonic wave is propagated in the vicinity of an open crack, the crack creates an echo whose amplitude can be measured to create an image of the crack [8]. Linear Elastodynamic Gradient Imaging Technique (LEGIT), was developed to quickly image cracks using a laser vibrometer. For this method, a crack is excited via ultrasonic waves and imaged by taking the gradient of the dynamic response in the frequency domain. Nonlinear Resonant Ultrasound Spectroscopy (NRUS) is another ultrasonic technique used in this study to detect (as opposed to image) the presence of a crack. NRUS was first developed to measure the nonclassical, hysteretic component of material nonlinearity by tracking the change in resonance frequency with increasing strain amplitude [9,10]. The next technique discussed, vibrothermography, also utilizes ultrasonic waves to excite a crack, however, the imaging methodology is based on heat generation [11]. As a crack is excited, the clapping of the crack faces generates heat, which in turn can be imaged with an Infrared (IR) camera [12]. Finally, measurements using synchrotron X-ray tomography are presented. Micro X-ray tomography is a non-destructive technique that utilizes the differences in phase contrast between the crack and the material [13]. The sample is rotated 360° and a series of 2-D X-ray projections are taken and reconstructed to produce a 3-D representation of the crack.

2. Sample Description and Optical Imaging of the Cracks

The multiple crevice assembly (MCA) method described in ASTM G4829 and previous studies [14-16] was adopted to study the crevice corrosion and stress corrosion cracking behavior of type 304-09A stainless steel. The sample used in this study is shown in Fig. 1. The 304-09A compression washer specimen (50×25×1.4mm) was fabricated from a wrought plate, with a through-hole geometry (6.8-mm diameter) in the center of the specimen (Fig. 2b). The test surfaces of the MCA specimen were ground with 600-grit, wet silicon carbide (SiC) paper and ultrasonically cleaned with methanol for a period of 10 minutes before the test. A mixture of NaCl and KCl (50:50) salts were deposited on the specimen surface via an airbrush with a methanol carrier (6 passes). The deposition density was measured as 99.1 ug/cm^2 with a quartz crystal microbalance (QCM) during deposition. Once deposited, the polytetrafluoroethylene (PTFE) tape covered ceramic crevice former was used to form the crevices. Each crevice former had 12 crevice contacts and the area of each crevice contact was 0.06 cm^2. The PTFE tape was standard military-grade thread sealant tape with an initial thickness of 76 µm. The crevice former is shown in Fig. 2a. The specimen and two crevice formers were assembled together with two grade 2 titanium bolts, nuts and washers, with an applied torque of 7.91 Nm (70 in-lbs). The titanium bolts, nuts and washers were electrically isolated from the specimen with the PTFE tape. Fig. 2b shows the MCA assembly with two crevice formers. The sample was then exposed to a 105 °C environment with a dew point of 95 °C for 100 days.

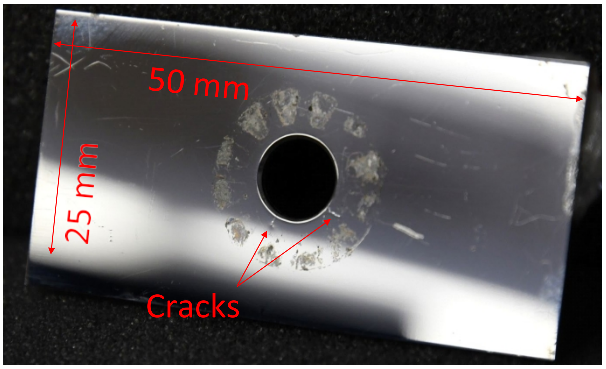

Fig. 1. Photograph of the sample used in the comparative study.

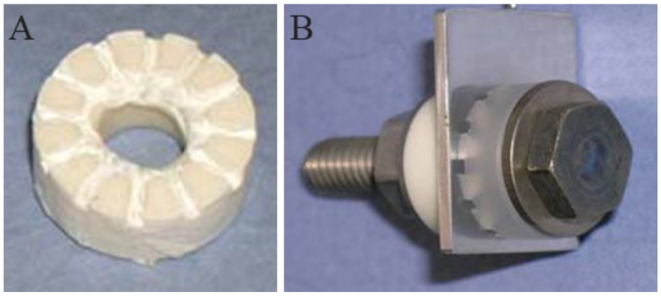

Fig. 2. (a) Ceramic crevice former, and (b) the multiple crevice assembly.

Optical observation of the crack on sample surface only show part of the whole crack along the radial direction of the hole (Fig. 3). The surface crack start to appear on the specimen surface at a distance of 463 μm away from the edge of the hole. Under optical microscope, the crack also appear at the middle region of the edge of the hole. Several pitting sites are found along the crack path, and more pits are found at other regions on the specimen surface. Large corrosion areas are found at the crevice contact regions. The corrosion area at the top left in Fig. 3 is a small part of the crevice contact region.

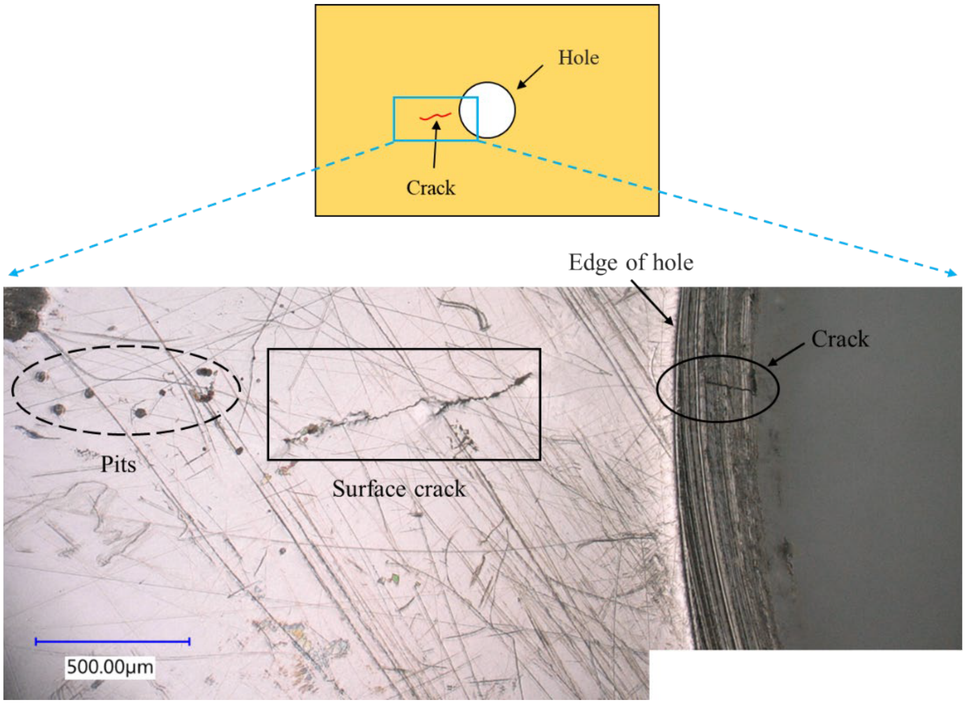

Fig. 3. Optical image of the crack and pits on sample surface. The schematic drawing is used for better understanding of the location of surface crack. Dash oval indicates some pitting sites, solid rectangle indicates surface crack and solid oval shows the crack in the middle region of the edge of the hole.

An enlarged view of the surface crack with a total length of 830 μm is shown in Fig. 4. Pitting sites are indicated with arrows. There are several pitting sites along the crack path. Fig. 4a shows two pits that are connected by the surface crack on the lower left side. Corrosion products are found around these pits. Two large crack deviation regions (Figs. 4b and c) and several small crack jumps (Fig. 5) are also found along the crack path; cracks in these regions are disconnected on the specimen surface under optical observation. The crack appears to originate from surface locations (pitting sites).

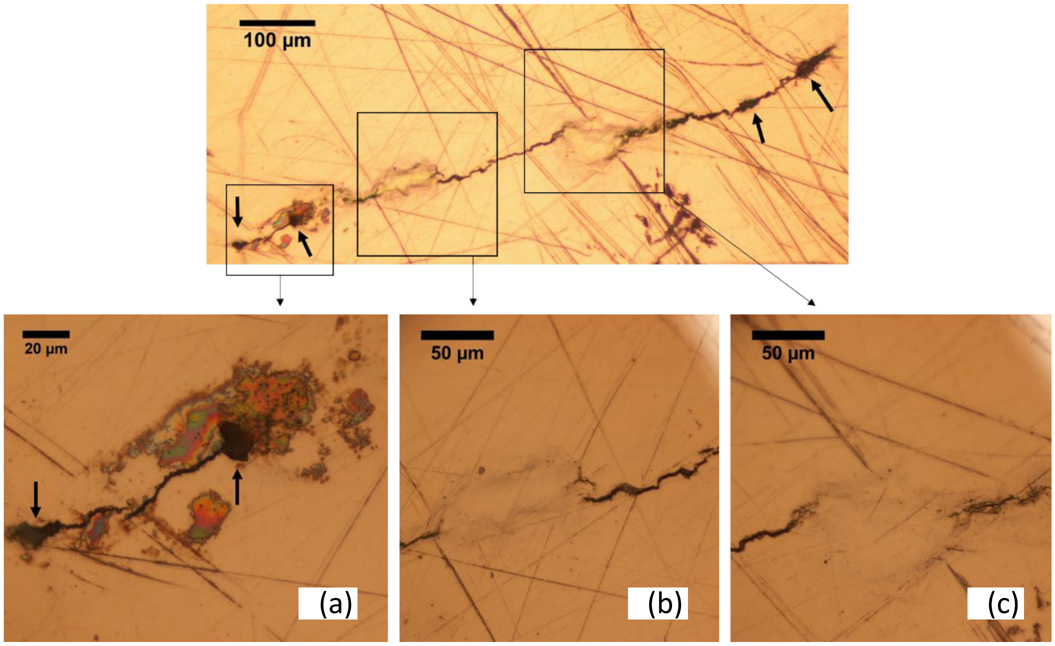

Fig. 4. Enlarged view of the surface crack, pitting sites and crack deviation regions. (a) Two large pitting sites along the crack path and corrosion products around the pits; (b) and (c) two large crack deviation regions along crack path.

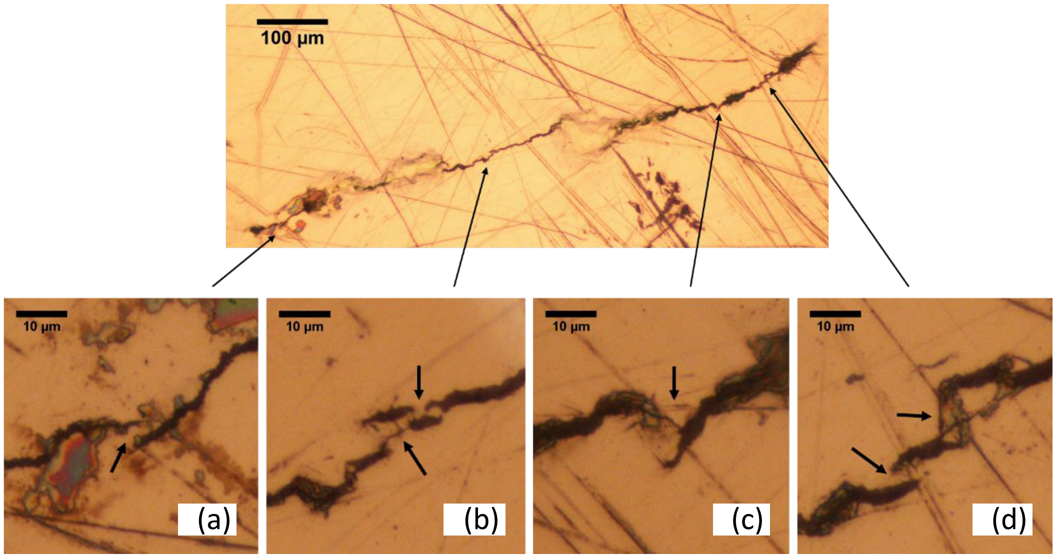

Fig. 5. (a)-(d) Small crack jumps along the crack path on sample surface.

3. Ultrasonic C-Scan

Ultrasonic testing that employs linear elastic-wave propagation in a sample has been widely used for the inspection of optically nontransparent materials such as metallic samples. Frequencies on the order of MHz are typically selected in contact testing, where the ultrasonic piezoelectric transducer are contacted to the specimen through liquid coupling gel [7,8,17]. Because this is a linear technique based on the scattering of the elastic waves by the defects, the wavelength used for testing should similar in size or smaller than the defect to be imaged. This requirement typically results in operating frequencies ranging from MHz to GHz for water (or other coupling liquid) immersion testing [18-23]. Note that C-scans cannot be conducted through air (with air-coupled transducers) because of the large attenuation and impedance mismatch between air and the sample at these frequencies. In this method, a sample is immersed in a tank with a liquid that is mainly water. In most cases, a geometrically focused transducer is employed to enhance both resolution and sensitivity. Ultrasound emitted from a focused transducer propagates in water to a sample and reaches the top surface of the specimen. When the focused transducer is placed so that a focal point matches just on the top surface of the specimen, the maximum reflection is obtained on the surface. As the focused transducer is moved close to the sample, the focal point is newly created within the sample. Due to the refraction of ultrasound at the top surface of the sample, the distance between the focused transducer and the focal point is shorter than the original focal length determined by the geometry of the focused transducer. The distance between the top surface of the sample and the newly created focal point within the sample is called defocusing distance. Ultrasound is most strongly influenced by defects when the defect exists in the vicinity of the focal point. The ultrasound influenced by the defect propagates back to the transducer, and it is received by the same transducer. By using a pulse wave with a temporal resolution, the echo from the defect may be measured separately to the other echoes from the top and bottom of the sample, which are even stronger than the defect echo. As the focused transducer is mechanically scanned with a fine pitch in a plane parallel to the sample surface, the amplitude of the echo is recorded at each scanning position. An image is created by two-dimensionally mapping the amplitude of echo, showing the defect distribution in the vicinity of the focal depth. The image is called C-scan. By repeating the same procedure at different focal depths, the C-scans can be obtained for different focal depths.

Fig. 6 shows the experimental setup for obtaining C-scan image of the sample. With respect to the selection of focused transducer, as described above, a high frequency is capable of achieving both high sensitivity and high resolution, whereas it loses the penetration depth due to the high attenuation. Practically, the tradeoff between resolution and penetration depth needs to be discreetly considered. In this study, the focused transducer with a center frequency of 50 MHz was selected. The diameter is 6 mm and the focal length determined by the geometry of curved surface of the transducer is 20 mm. The sample was immersed in a water tank, and the focused ultrasonic transducer was partially immersed for normal incidence. The focused transducer was excited by a pulser (DPR500, JSR), which was controlled by a scanning and acquisition system (FlexScan, Insight, Japan). In this study, the cracks were indirectly visualized via the amplitude of bottom echo to achieve a high signal-to-noise ratio, since the direct scattering from the cracks was too small. In order to acquire C-scan images at various depths within the sample, the focal point was varied from the top surface of the sample to the bottom. For each defocusing distance, the mechanical scan was carried out over 20 x 20 mm^2 with a pitch of 0.1 mm. At each depth, the scan time for such a grid is on the order of minutes.

Fig. 7 shows the C-scan images obtained at different focal depths with the schematic illustrations. At the focal position on the top surface of the sample (Fig. 7a), multiple point-like responses were imaged in the area surrounding by the central hole (Fig. 7f). Most of them can be attributed to the small pits and rough surface due to local corrosion, since the positions of most responses were in good agreement with the positions of optically-observed ones. Although some of them may be attributed to small SCCs, it is not easy to identify them only in the C-scan image. As the focal position is moved toward the bottom surface of the sample (Figs. 7b-e), the multiple point-like responses became weak and ambiguous at the same positions in the C-scan images (Figs. 7g-j). For the deep focal points, some of them diminished. This is because the focal points were away from the top surface. This clearly shows that such scatterers existed only on the top surface of the sample. On the other hand, two SCCs extending from the central hole were clearly visualized as linear-shaped responses. In contrast to the aforementioned surface scatterers, the two SCCs were visualized consistently over all the focal depths within the specimen. This suggests that the SCCs penetrate through the thickness. Note that in Fig. 7i, the SCC2 was visualized as wider linear-shaped response**.** In Fig. 7j, SCC2 was observed as two linear responses. The results may suggest that SCC2 was slightly tilted or was branched around the surface A. Additionally, a third line is observed on the edge of the hole. For this line, the contrast in the image does not appear to be as strong as the other two lines (SCC). Further inspection reveals that this third line is a scratch but without additional testing, this third line could have been a false positive for SCC.

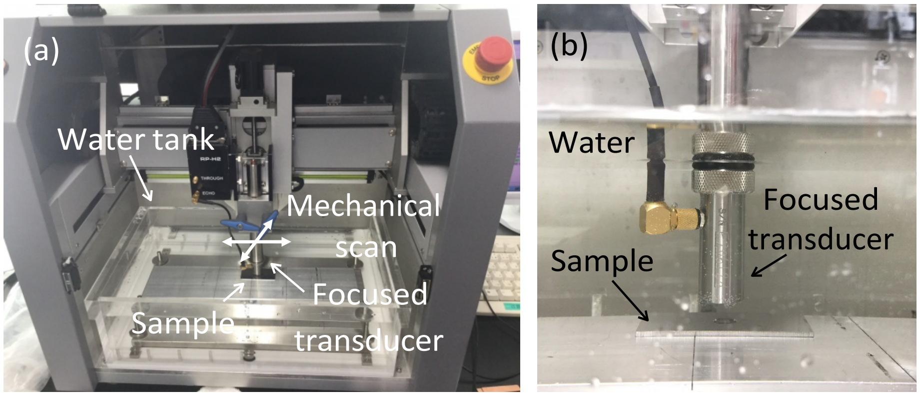

Fig. 6. Experimental setup for ultrasonic C-scan images: (a) A tank with water where a focused transducer and the sample are immersed. (b) An enlarged photograph from the front that shows the appearance of ultrasonic focused transducer and the sample in a water tank.

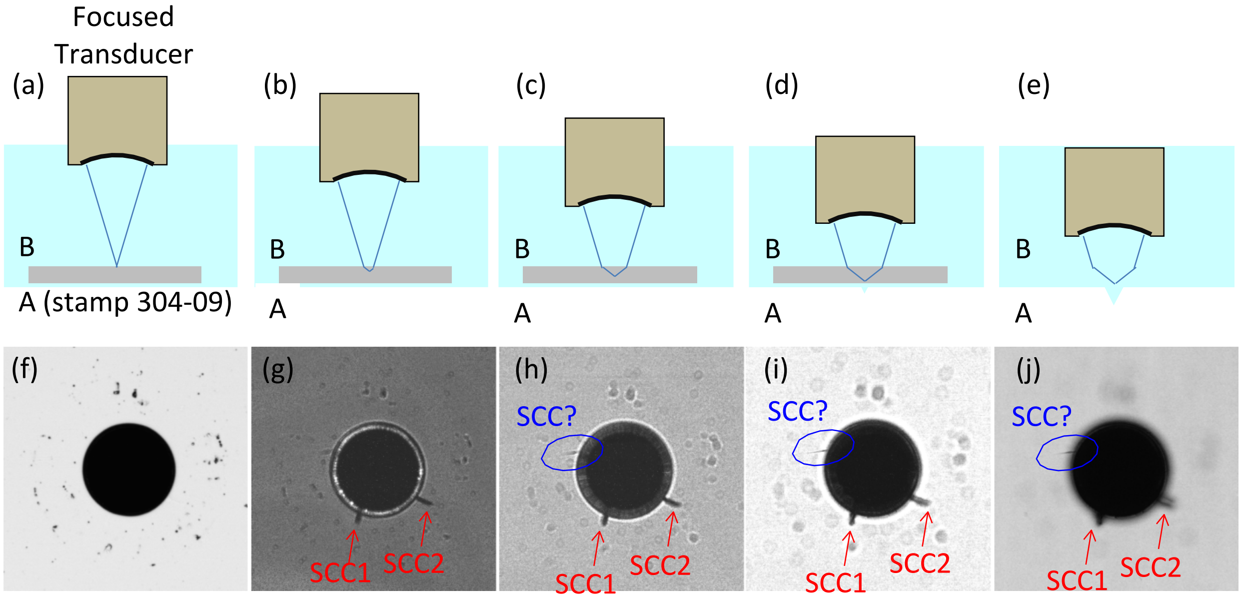

Fig. 7. C-scan results obtained at various focal depths at 0.5-mm depth increments: (a)-(e) Schematic illustration showing the focal points on and within the sample. (f)-(j) Ultrasonic C-scan images obtained at the focal points shown in (a) to (e), respectively.

4. Detection Using Nonlinear Resonant Ultrasound Spectroscopy (NRUS)

Elastic waves are useful for nondestructive testing (NDT) applications because they are carried by the solid and interact with its constituents, including its defects. Imaging techniques based on linear ultrasonics (e.g., amplitude C-scan in Section 3) rely on the idea that ultrasonic waves are scattered by the defects, which alter the expected time of flight of the incident wave and/or its amplitude. These techniques typically require that the wavelength be smaller than the defect and that the defect create a large enough contrast of impedance within the solid. In this subsection, we focus on different effects, those stemming from nonlinear elasticity. Many material defects lead to nonlinear effects during the propagation of finite-amplitude ultrasonic waves, manifested as wave distortions in the time domain or generation of harmonics in the frequency domain [24-26]. Unlike techniques relying on linear scattering, these effects may be observed even when the wavelength is much larger (by orders of magnitude) than the defects. This fact is of practical importance for NDT applications since it may be and has been used for the early detection of defects in materials. In fact, it has been demonstrated that nonlinear signatures are far more sensitive to the presence of microscopic-sized defects, which are precursors to larger defects and eventually system failure, than linear signatures, including linear scattering, changes in the propagation speed of the ultrasonic waves, and linear attenuation [25,26].

NRUS is used in this study as a preliminary screening tool, to indicate whether or not a sample is damaged. Basically, NRUS consists of (i) vibrating a sample of finite size around one of its resonance frequencies at multiple amplitudes and (ii) tracking the dependence of the resonance frequency on the excitation amplitude. The resonance frequency of a pristine metallic sample should be independent of the excitation amplitude, as long as the maximum dynamic strain amplitude in the sample remains within the range of linear elasticity for the material studied. In the presence of cracks, dislocations, thermal damage, and possibly other defects, the resonance frequency starts decreasing as a function of strain, and very noticeably so when the strain goes above a certain level, typically near 10^{-6} at ambient conditions. Such a behavior has been observed in a variety of materials, including metals, rocks, and concrete. Broadly speaking, the drop in resonance frequency indicates material softening with increasing driving strain. However, the dependence of the resonance frequency on strain is not trivial [10,27] as it involves different mechanisms of nonlinearity (i.e., classical and nonclassical) at various strain amplitudes. Of interest to this study is also the fact that the strength of the nonlinear response (e.g., dependence of the resonance frequency on vibration amplitude) is proportional to the crack density in the sample, as demonstrated by Van Den Abeele et al. [28] using thermally damaged composite samples. Hogg et al. [29] also recently found that α increases in welded steel rods with longer exposure to a hot, corrosive, aqueous $MgCl_2$ environment due to the suspected increase in SCC nucleation and growth with longer exposure.

In some previous studies conducted by some of the authors, the sample was a long thin bar with free boundary conditions and excited around the first mode of longitudinal vibration. The equation of motion and boundary conditions for the longitudinal modes of the bar of length L ($-L/2 \le x \le L/2$) and mass density ρ can be expressed as,

$$\rho\frac{\partial^2 u(x,t)}{\partial t^2} = \frac{\partial}{\partial x}\left[E(x)\frac{\partial u(x,t)}{\partial x}\right],\ \varepsilon_{xx}\left(\pm {}^{L}/_{2}\right) = 0 \tag{1}$$

where $u(x,t)$ is the displacement of the bar in the longitudinal (x) direction and $E(x)$ is the Young's modulus, which varies with position x due to the presence of nonlinearity that depends on the strain $\varepsilon_{xx} = \partial u\left(x,t\right)/\partial x$.

In this paper, the sample has a complex geometry and set into complex motion by a contact transducer that is relatively large. The ideal conditions described by Eq. (1) are not met. However, damage detection is the priority in the study (rather than modeling the fine details of the physics leading to the nonlinear elastic behavior) and the key aspect of the experiment is to find a mode of vibration capable of exciting the damaged region. Such a mode of vibration can involve a longitudinal, torsional, and/or bending motion, as long that the cracks are set into motion to generate the sought nonlinearity.

NRUS experiments were conducted on two samples, the one shown in Fig. 1 with the two SCCs and another sample of identical shape in pristine conditions (without SCC) to be used as a reference. The experimental setup is shown in Fig. 8. A piezoelectric disc (PZT-5A ceramic with a diameter of 12.7 mm and a thickness of 2 mm) was epoxied near one corner of the sample and used as a source transducer to vibrate the sample. The transducer was driven with voltage signals generated by a function generator (National Instrument PXI-5406) and amplified 20 times by a voltage amplifier (TEGAM 2350). The vibrational response of the sample was measured with a laser Doppler vibrometer (laser head: Polytec PSV 400; vibrometer controller: OFV-5000; Decoder: VD-09 with max range of 200 mm/s/V and max frequency of 250 kHz) near another corner of the sample. The vibrational signals were digitized with a sampling rate of 10 MHz (National Instrument PXI-4122). The samples were vibrated with a sequence of harmonic voltage signals (i.e., sinusoidal bursts) around their fourth resonance mode with a frequency bandwidth of 100 Hz in steps of 2 Hz: from 7.48 to 7.58 kHz for the pristine sample and from 7.82 to 7.92 kHz for the sample with SCC. Each harmonic signal was played for 80 ms and the transient vibrational response was recorded during the last 40 ms of the source signal, to ensure that steady state conditions had been reached at each frequency step. Vibrational spectra were constructed from the harmonic responses, using heterodyne processing. The experiment was conducted for 24 excitation amplitudes ranging between 0.25 to 6 Vpp in steps of 0.25 Vpp, before amplification.

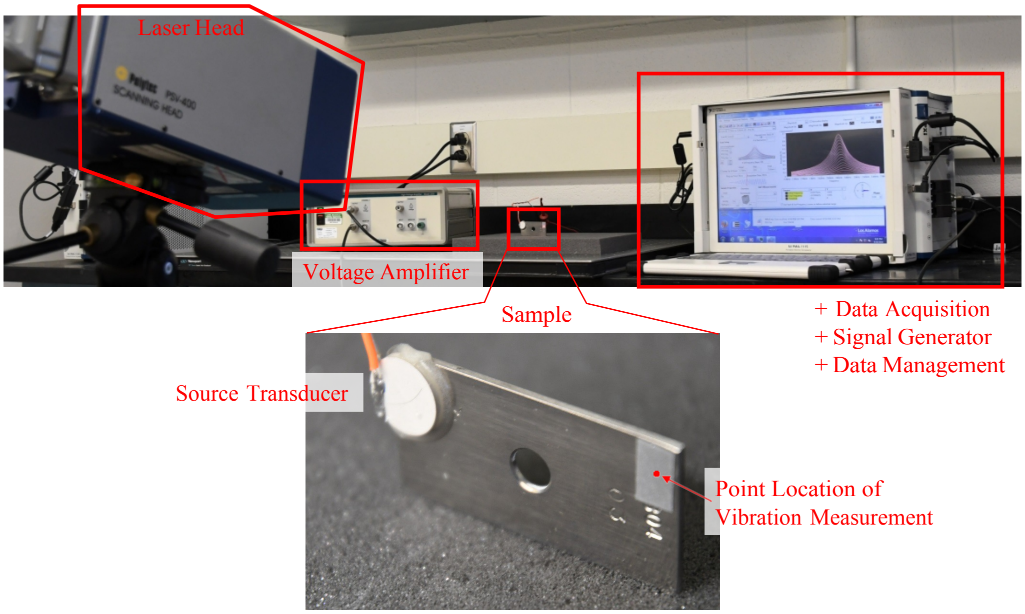

Fig. 8. Photograph of the experimental setup for NRUS measurements.

The resonance curves for the two samples are shown in Figs. 9a and b. Both samples exhibit a shift of their resonance frequency as a function of the source amplitude. It is also clear that the sample with SCC exhibits a more pronounced shift of its resonance frequency than the pristine sample. The first result is expected as all dynamic systems will eventually behave nonlinearly at sufficiently large dynamic amplitudes. In this case, the piezoelectric transducer and epoxy bonding between the transducer and the sample are most likely the cause of the nonlinearity (shift of resonance frequency) observed in the pristine sample. The second result is caused by the presence of SCC.

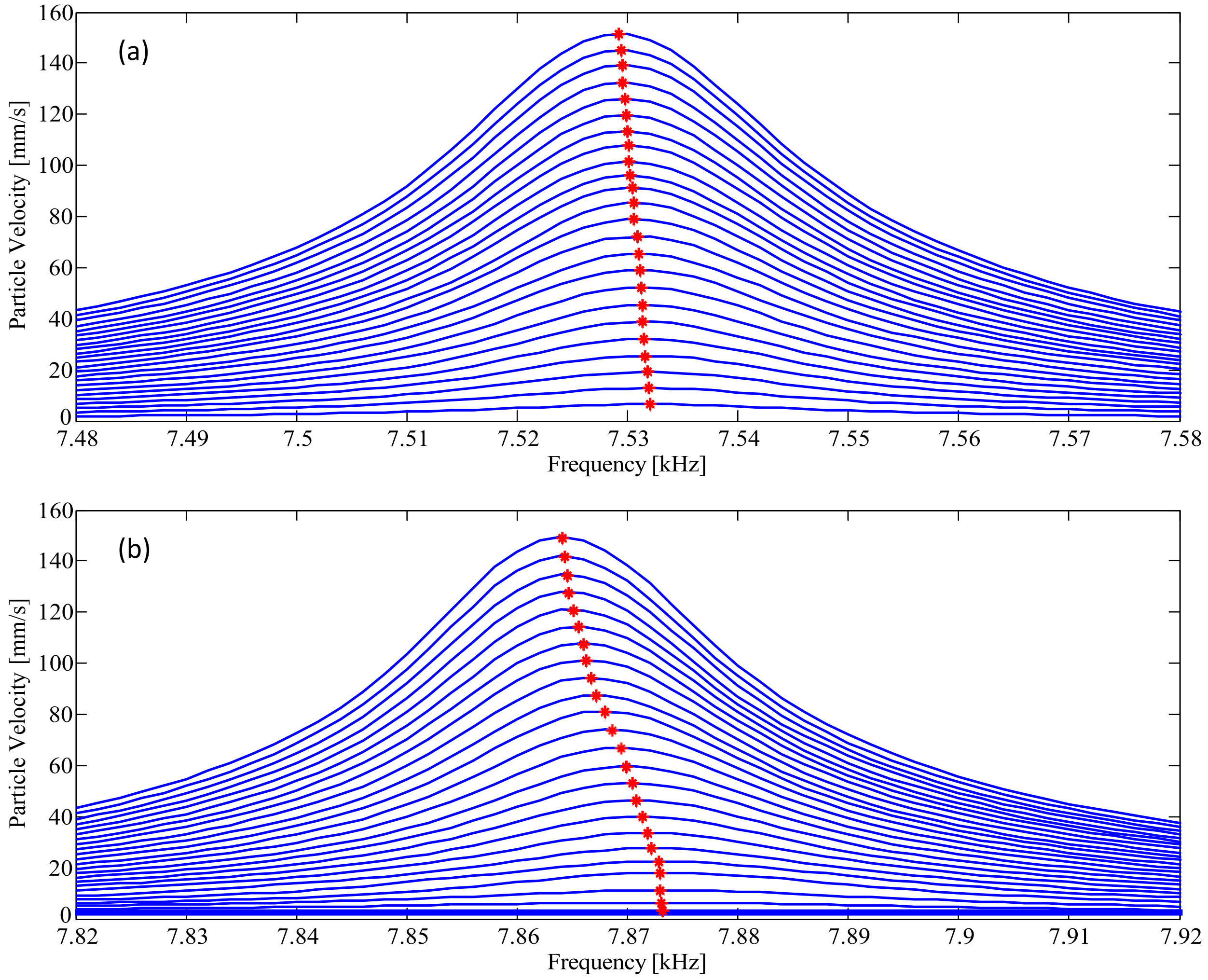

Fig. 9. Magnitude of the spectra of the particle velocity measured for 24 source amplitudes around the fourth resonance mode of vibration of the sample: (a) pristine sample; (b) sample with SCC.

Quantification of the nonlinearity is done by analyzing the relative shift of the resonance frequency as a function of the maximum amplitude of the volumetric strain in the region of interest (the boundary of the hole at the center of the sample). In the experiments, the vibration is measured at one point only. The relationship between the particle velocity at that point and the maximum strain amplitude is established with numerical modeling, based on the finite-element (FE) method implemented in the commercial software package COMSOL Multiphysics. The FE model consists of the sample instrumented with the source transducer, with geometry and material properties shown in Fig. 10. The computational domain is discretized into 34770 quadratic tetrahedral elements with a maximum element size of 0.9 mm, resulting in a model with 171996 degrees of freedom. The first 5 resonance frequencies and corresponding mode shapes of the sample were computed. Fig. 11 shows the magnitude of the displacement and volumetric strain for these modes. A frequency sweep was also conducted experimentally between 1 and 11 kHz to identify the resonance frequencies and check the validity of the model. The spectrum measured in this experiment is shown in Fig. 12. The agreement between measured and predicted resonance frequencies is excellent considering that the epoxy (bonding between transducer and sample) was not modeled and nominal (as opposed to measured) material properties were used in the simulations. The numerical model indicates that the ratio of the particle velocity at the measurement point (where the laser beam is pointing) and the volumetric strain at the boundary of the center hole (where the cracks are located) is approximately equal to 18000 m/s.

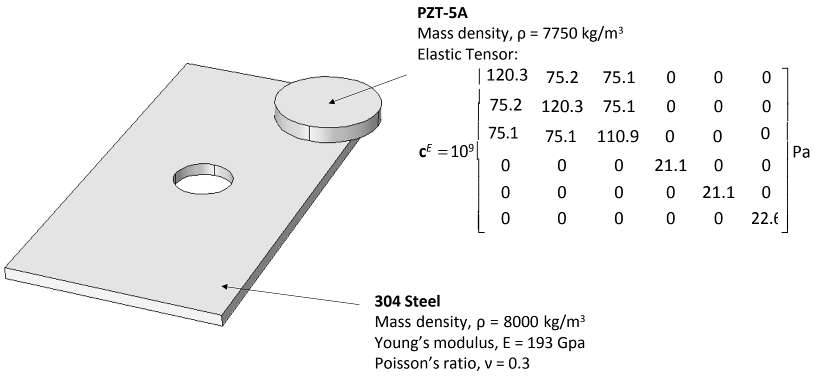

PZT-5A
Mass density, ρ = 7750 kg/m^3
Elastic Tensor:

$$\mathbf{c}^E = 10^9 \begin{bmatrix} 120.3 & 75.2 & 75.1 & 0 & 0 & 0 \\ 75.2 & 120.3 & 75.1 & 0 & 0 & 0 \\ 75.1 & 75.1 & 110.9 & 0 & 0 & 0 \\ 0 & 0 & 0 & 21.1 & 0 & 0 \\ 0 & 0 & 0 & 0 & 21.1 & 0 \\ 0 & 0 & 0 & 0 & 0 & 22.6 \end{bmatrix} \text{Pa}$$

304 Steel
Mass density, ρ = 8000 kg/m^3
Young's modulus, E = 193 Gpa
Poisson's ratio, ν = 0.3

Fig. 10. Geometry of the model and material properties used to compute the resonance frequencies and corresponding mode shapes of the sample instrumented with the source transducer.

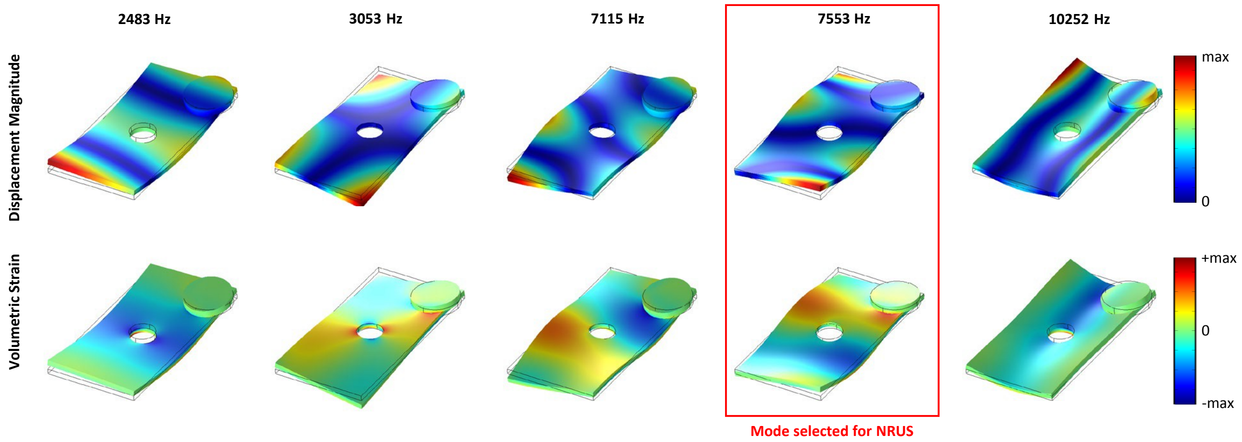

Fig. 11. First five resonance frequencies and corresponding mode shapes of the sample instrumented with a source transducer.

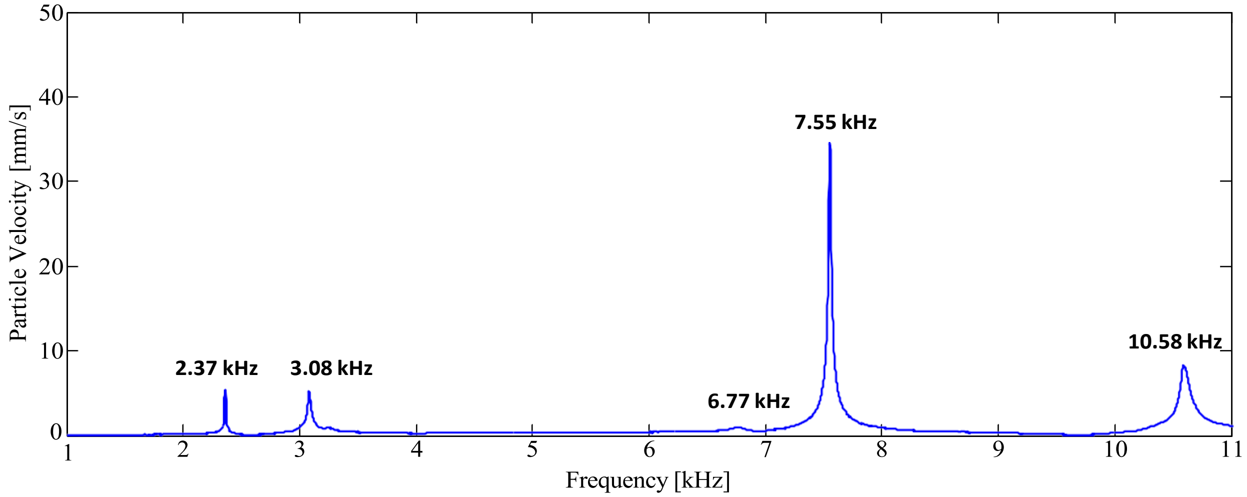

Fig. 12. Magnitude of the spectrum of the particle velocity measured near a corner of the sample for low-amplitude source signals. A low-amplitude source signal ensures that the vibrational response is linear.

Using the results from the numerical analysis, it is now possible to reduce the data plotted in Fig. 9. The relative shift of the resonance frequency as a function of the volumetric strain (estimated at the boundary of the center hole) is shown in Fig. 13 for the two samples. The slope of the linear portion of the data is the parameter of nonclassical nonlinearity α. For the pristine sample, α = -45. For the sample with SCC, α = -185, which represents an increase by a factor of 4 compared to the pristine sample. Given that the samples had the same geometry, were instrumented with the same transducers, and were driven with the same signals, this large increase can only be attributed to the presence of cracks.

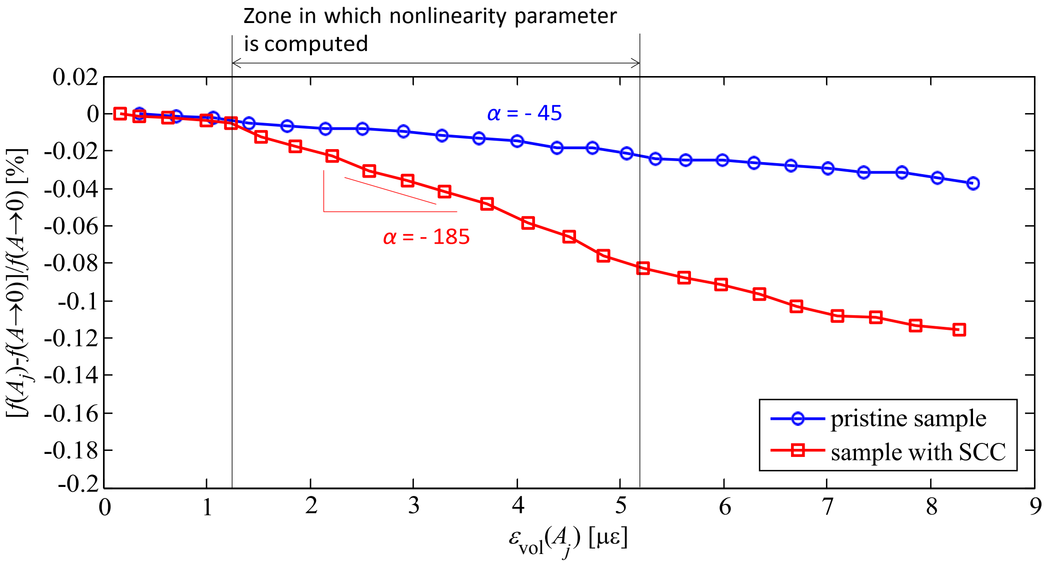

Fig. 13. Magnitude of the spectrum of the particle velocity measured near a corner of the sample for low-amplitude source signals. A low-amplitude source signal ensures that the vibrational response is linear.

In the intended application of using NRUS to detect the presence of SCC on a storage cask, NRUS measurements can be made with the same equipment, over regular time intervals, to determine whether α is increasing with time or not. It is likely that experiments conducted on pristine casks and then on damaged casks may be needed to help quantify the α value, which, if exceeded, will suggest the presence of SCC, though perhaps numerical models can provide this information as well. Since NRUS requires the measurement of resonance curves at several amplitudes, including low enough amplitudes to assume linear elasticity, changes in the overall wave speed in the sample are taken into account. Thus the NRUS technique does not rely as heavily on the direct comparison to a pristine sample nor does it depend on the sample's wave speed remaining constant, but rather α depends on the quantity of cracking present, as previously discussed [28,29]. Note that in principle, NRUS may be used for crack localization, as suggested by Abeele [30] and demonstrated by Ohara et al. [31]. In brief, the localization of nonlinear scatterers can be achieved by changing the mode order, thus changing the location of the nodes and anti-nodes of vibration. While this is a relatively simple process for small samples with simple geometries, it could become a daunting task if the crack size is orders of magnitude smaller than the host structure and the geometry of the structure is complex.

5. Linear Elastodynamics Gradient Imaging Technique (LEGIT)

As part of this study, a new technique was developed, namely, Linear Elastodynamics Gradient Imaging Technique (LEGIT). For LEGIT, a transducer inputs acoustic energy into the sample in the form of a pulse. The interaction of the cracks in the sample with the acoustic waves results in discontinuities at the crack locations, which can be imaged by measuring the response of the sample using a laser vibrometer.

The experimental set-up is shown in Fig. 14. A piezoelectric transducer (PZT-5A ceramic with a diameter of 12.7 mm and a thickness of 2 mm) was epoxied near a corner of the sample. Reflective tape was applied to the sample over the region where the two SCCs were known to be located to increase the Signal to Noise Ratio (SNR). The input signal was generated from an internal arbitrary waveform generation card in the scanning laser vibrometer (Polytec PSV-3D-500 in 1D mode). The signal was then amplified 100 times by a voltage amplifier (TEGAM 2350) before being input to the piezoelectric transducer.

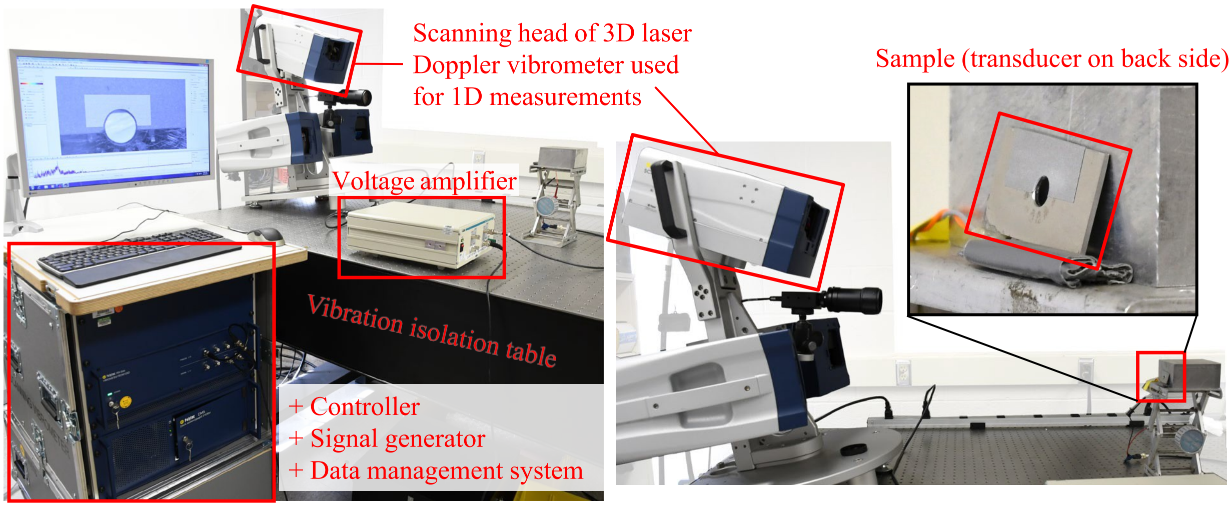

Fig. 14. (Left) Entire experimental set-up for LEGIT with data acquisition system shown. Only the top laser head was used to measure the out-of-plane velocity component. (Right) Side view of experimental setup showing the sample, inset is a close up view of the sample. The piezoelectric transducer is not visible because it is on the backside of the sample.

To maximize the response of the sample, the input signal was centered around one of the resonance frequencies of the sample. The resonance peaks of the sample were found by inputting a burst chirp with frequencies from 20 kHz to 300 kHz into the sample and observing the response at various locations on the sample. An example of a frequency spectrum from a point on the sample is shown in Fig. 15. Based on the measured spectrum, a pulse at 175 kHz with 157 cycles was chosen as the input signal.

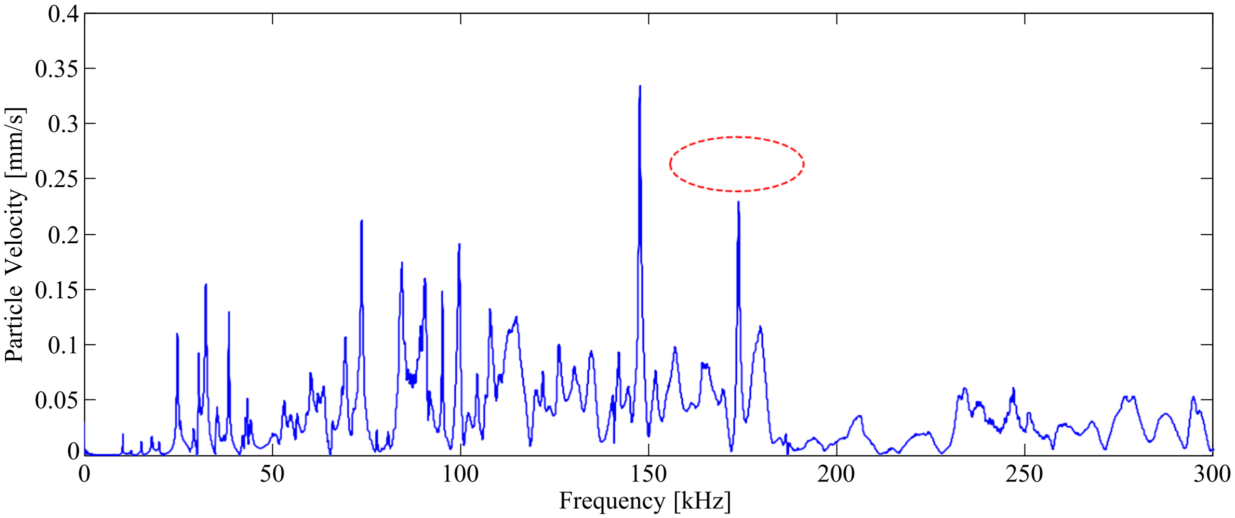

Fig. 15. Frequency spectrum for input pulse with frequencies from 20 kHz to 300 kHz. The resonance frequency of 175 kHz was chosen as the frequency for the input signal.

Using the Polytec acquisition software, a scan grid was defined around the region with the two SCCs. Fig. 16 shows the defined scan grid. The grid contained 6516 points and was 15.5 mm in length by 7.2 mm in height, resulting in a resolution of approximately 0.12 mm. At each point on the scan grid, the pulse was input into the sample and the out of plane velocity response was measured using the scanning laser vibrometer (Polytec PSV-3D-500 in 1D mode). Only the top laser head was used to measure the out of plane velocity component. Data was collected at 3.25 MHz for 10 ms. Each pulse was allowed to dissipate before moving to the scan point.

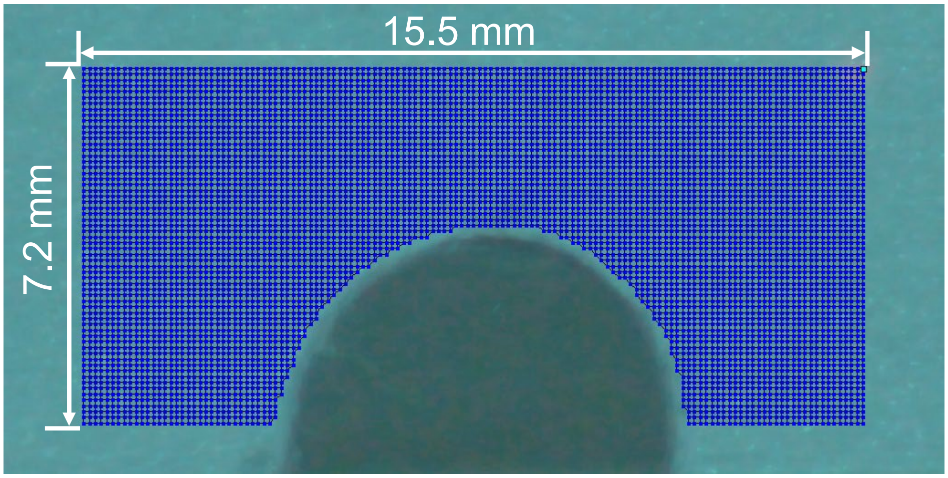

Fig. 16. Scan grid with 6516 points, with a resolution of approximately 0.12 mm.

To process the data, the time domain data was taken to the frequency domain. Fig. 17 shows a frequency spectrum from one point on the scan grid. The spectrum was integrated around the fundamental mode at each point on the scan grid to build an image of the defect locations. Next, the gradient was taken in the *y*-direction to identify the discontinuities caused by the interaction of the SCCs with the acoustic waves (Fig. 18a). As can be seen in Fig. 18c, comparing LEGIT results to that obtained with vibrothermography (Fig. 18b) (see Section 5), shows the identified crack locations are in agreement.

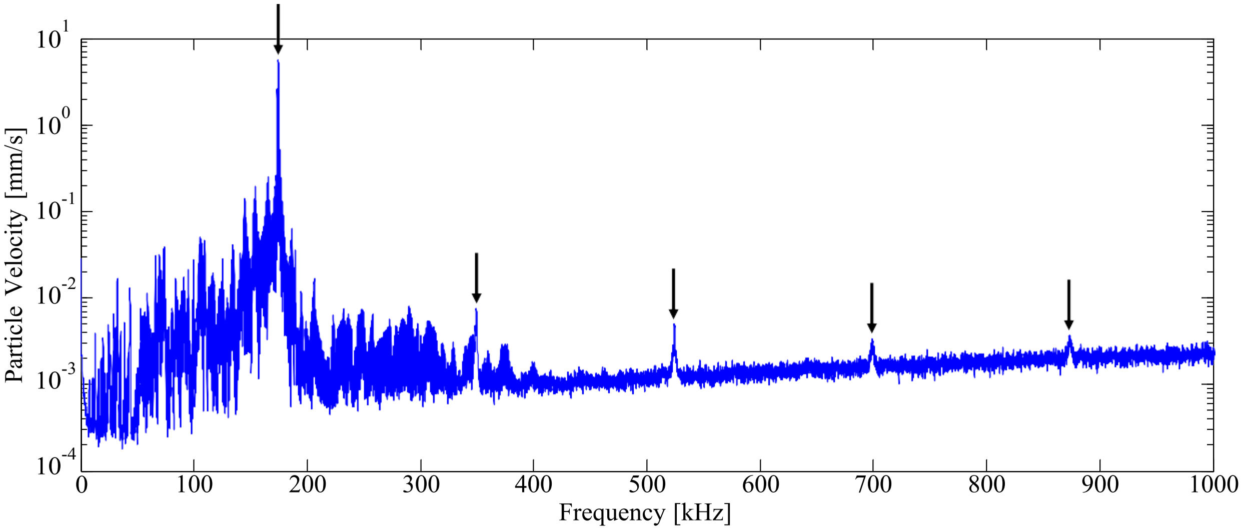

Fig. 17. Frequency spectrum for one point on the scan grid, harmonic generation from the SCCs is evident in the spectrum.

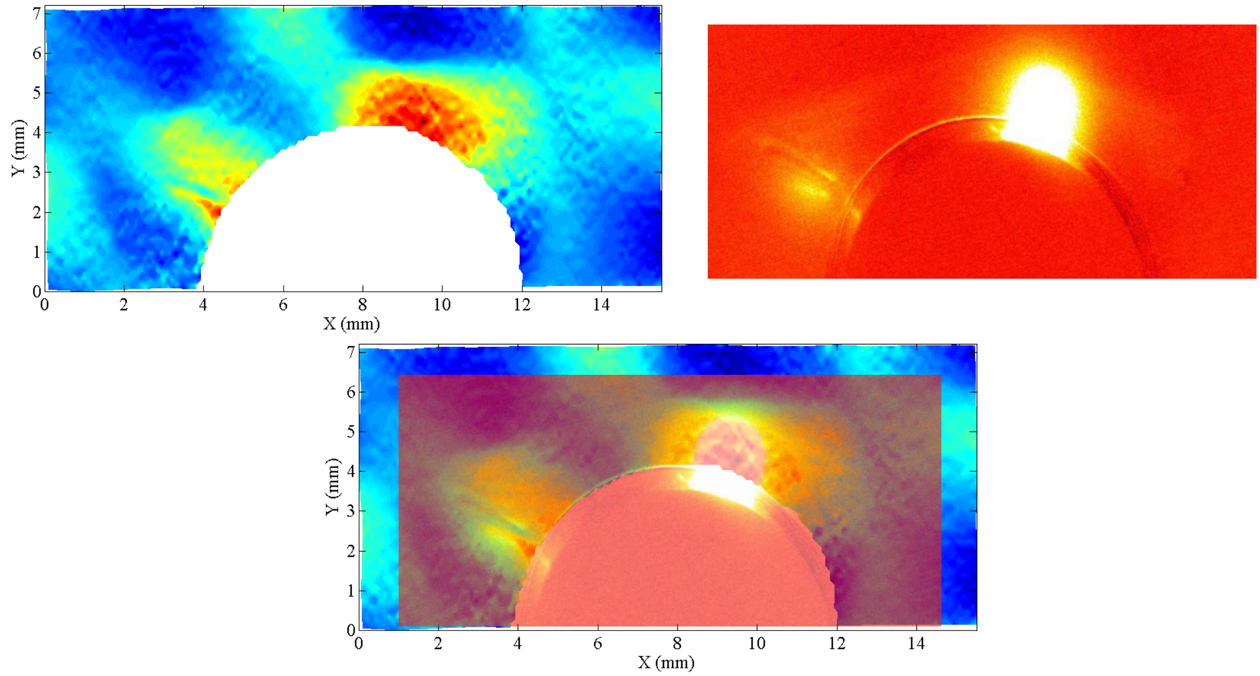

Fig. 18. Results from LEGIT (a) image from taking the gradient in the *y*-direction of the integrated fundamental frequency. The large red area and the discontinuity on the left side of the hole correspond with the crack locations from vibrothermography (Section 5) (b). Overlaying the image from LEGIT and the vibrothermography (c) shows that the identified SCC locations agree well.

6. Vibrothermography

Vibrothermography is a NDE method used to detect surface and near surface defects in materials. While this method was first used to find cracks and delaminations in composite materials [11], its applications have since been expanded to detect cracks in metals [32]. Vibrothermography offers advantages in that it is able image large areas for cracks efficiently. In order to standardize vibrothermography, work is being done to understand the effects experimental variables have on the probably of detecting a defect [33].

Vibrothermography utilizes the conversion of mechanical energy to heat to image damage. At defect locations, heat is converted to mechanical energy. The physical heat-generating mechanisms of cracks are frictional heating from crack faces rubbing and/or clapping, plastic deformations from crack growth, and viscoelastic heating due to stress concentrations in a material. Friction as a heat-generating mechanism has been supported by numerical models that couple thermomechanical analysis to predict the temperature distribution on fatigue cracked steel samples [34]. Renshaw et al. have confirmed all three of these heating mechanisms through experiments that isolated each mechanism for careful individual study [12]. Viscoelastic heating, however, has been found to be a dominant mechanism in polymer based composite materials [11], and therefore is not considered a dominant heat generation mechanism in the current study. It is also important to note that friction can induce plastic deformation along a crack as the faces are being clapped together. The amount of heat generated is influenced by the external stress state and whether the crack is open or closed. As the external stress is increased, experiments have shown that heat generation moves to the edges of a crack [35]. If a crack is fully open or fully locked by external stress, vibrothermography will likely not detect the crack due to lack of heat generation.

To image defects with vibrothermography, samples are resonated using a mechanical excitation device, e.g. piezoelectric transducers, electromagnetic shakers, or ultrasonic transducers, and imaged with an infrared (IR) camera. In the current study, a piezoelectric transducer was epoxied to a corner of the sample following the setup used for the NRUS testing (see Fig. 8). A frequency sweep over a wide frequency band indicated that the maximum vibration amplitude was reached near 175 kHz. This frequency was selected for the test to create the maximum thermoelastic effect while ensuring that the sample would remain in the elastic regime and the crack would not grow further. The infrared emission in the region of interest was recorded for 10s at 120 frames per second using a FLIR SC8200 IR. The source transducer was driven at 200Vpp for 7.5s, 0.5s after the acquisition had started (for the last 2s of the acquisition, the source was off). The data acquisition and processing were controlled by a system (hardware + software) developed by Thermal Wave Imaging. It takes less than 30s between the start of the experiment and the completion of the data post-processing displayed below.

Fig. 19 shows 3 snapshots of the thermal field in the region of interest. Some data processing is required to obtain these images. The camera originally provides a map of the temperature distribution for each frame of the video acquisition. The evolution of temperature with time, $T(t)$, is noisy. Noise is removed by fitting $T(t)$ with a 10th-order polynomial at each data point of the map. The contrast is then enhanced by taking the first derivative with respect to time of the fitted $T(t)$. Any abrupt change in temperature will be enhanced by taking the derivative. The evolution of temperature as a function of time at three points on the sample is shown in Fig. 20.

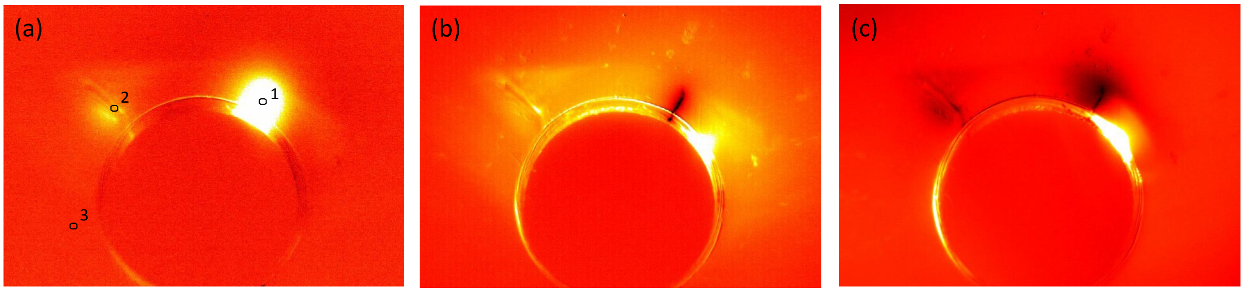

Fig. 19. Snapshots of the first derivative with respect to time of the temperature at each point of the scan region due to a continuous sine wave at 175 kHz. Snapshots taken at (a) 0.5s, (b) 4.5s, and (c) 9.5s into the 10s acquisition.

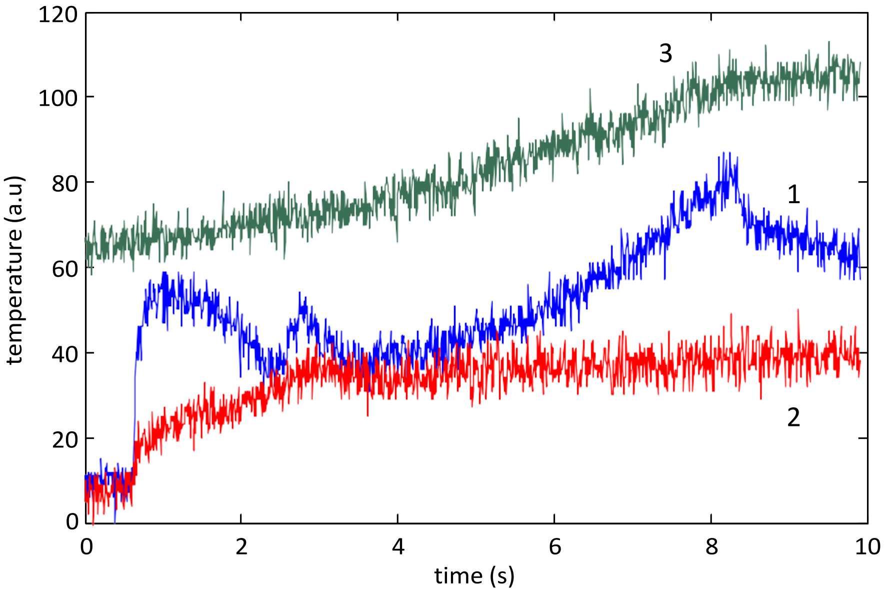

Fig. 20. Evolution of temperature as a function time at three points in the scan region. The location of the points (1,2,3) is indicated in Fig. 10(a).

7. Synchrotron X-ray tomography

X-ray tomography is used in this study to provide “ground-truth” measurements. The technique of X-ray tomography is similar to Computerized Tomography (CT) scans used in the medical industry to produce 3-D representations of the body [36]. A sample is rotated around an axis perpendicular to the high energy beam of X-rays and a series of 2-D projections are collected at the different angles of rotation [36]. The detectors are usually composed of a scintillator material along with a CCD camera [36]. The high brilliance of high energy X-rays allows for quicker scans compared to other X-ray tomography sources such as tungsten filament [37]. A filtered back-projection algorithm is then used to create 2-D images from the projections based on differences in phase contrast [36]. Phase contrast can arise from differences in X-ray absorption which can be altered by differences in materials, holes, cracks, and pores [37]. Further filtering using Fast Fourier transforms can be used to remove artefacts [38]. The 2-D images are then stacked and 3-D representation of the crack can be produced using a reconstruction software like Avizo ®. Various researchers have shown how X-ray micro tomography can be used to create 3-D representations of cracks with resolutions on the order of microns [13, 37, 39].

Although X-ray micro tomography allows for the 3-D reconstruction of cracks in materials with micron level resolution, this technique still has its limitations. Some of the limitations arise from the technique of phase contrast while others arise from the limited resolution. Features of the crack, which can include small secondary cracks and sharp crack tip, can be missed in the tomography scan due to their small size relative to the resolution of the scan [40]. Crack tip geometry is an important parameter for understanding crack propagation so lacking the insight into the crack tip radius can hinder a better understanding [40]. Additionally, cracks with large differences in aspect ratio can lead to unequal contrast at different projection angles which reduces resolution of the crack [40]. With regards to the technique of using synchrotron X-rays and using phase contrast, small samples (<10 mm) must be used to allow enough X-rays to pass through the sample [40]. Generally, samples must contain a square or circle cross section to avoid drastic changes in contrast with rotation [40]. From the parallel beam of X-rays, crack edges can cause fringes in the image to appear, resulting in a reduction of resolution in the area [41]. The formation of artifacts in the tomography scans adds additionally limitations to the technique [38]. Artifacts arise due to the non-linear response of the detectors as well as dust that can accumulate on the optics or scintillator due to the constant bombardment of high energy photons on materials [38]. Careful analysis of the scans is needed to identify artifacts that usually appear as rings in the 3-D model [38]. For in-situ scans involving various equipment, wobbling of the sample can become more common during the rotation of the sample which can lead to blurry areas in the sample if not corrected [42].

7.1 Microstructural Characterization

The morphology of cracks and pitting sites were inspected by optical microscopy and SEM (FEI Quanta 3D FEG). Elemental composition around surface crack and pitting sites were also determined by Energy-dispersive X-ray Spectroscopy (EDS), using an X-ray detector (Oxford Instruments) coupled with SEM. EDS, when combined with these imaging tools (SEM), can provide spatially resolved elemental analysis from areas as small as 0.1 ~ 3 microns. The impact of the electron beam on the sample produces X-rays that are characteristic of the elements present on the sample. EDS analysis was used to map out the lateral distribution of elements from the imaged area on the sample surfaces. In an EDS map, bright zones indicate enrichment of an element, whereas dark zones shows depletion of that element.

7.2 X-ray Microtomography

The microtomography experiment was conducted at the high-energy synchrotron beamline 1-ID-E at the Advanced Photon Source (APS) at Argonne National Laboratory (ANL), with a beam size of 2.1×1.3 mm. Measurements were collected with a monochromatic synchrotron X-ray beam at an energy of 90.55 keV. The specimen was mounted on a rotational stage that enabled the specimen to be rotated through a continuous 360° range with radiography collections 0.2° intervals along the rotation axis. The sample stage and detector were carefully calibrated to yield pixels rows perpendicular to the rotation axis of the sample, which facilitates reconstruction. This series of projections was reconstructed with a filtered back projection algorithm to obtain a dataset of a 3D isotropic voxels (size 1×1×1µm) representing voxel-average X-ray linear absorption coefficient. For the full crack, two vertical sample volumes were stacked.

Indeed, since the sample volume containing the full size of the crack cannot be included in one tomographic scan, two groups of tomography datasets (with partial overlapping) containing partial of the same crack were measured.

Fig. 21a is a schematic drawing of the SS304-09A compression washer with a through-hole geometry which shows two cracks. Fig. 21b shows the 3D iso-surface rendering of two layers (layer-1 and layer-2) of the crack on the top of the hole. These 3D image datasets with partial overlapping are then matched based on image registration to form a larger sample volume containing the full crack.

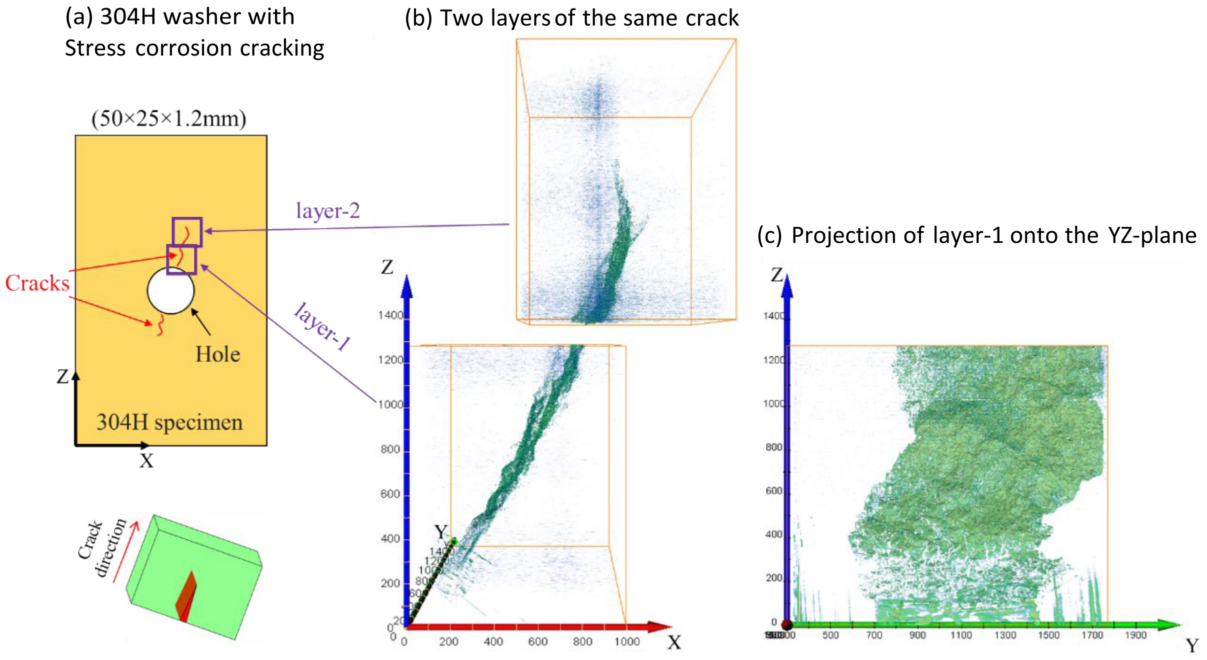
(a) 304H washer with Stress corrosion cracking

(b) Two layers of the same crack

(c) Projection of layer-1 onto the YZ-plane

Fig. 21. Tomographic scan of crack in SS304-09A compression washer. (a) Schematic drawing of a SS304-09A compression washer with a through-hole geometry (6.8mm diameter) and two cracks. (b) 3D isosurface rendering of two tomographic datasets (with partial overlapping) of the same crack. (c) Projection of layer-1 onto the YZ-plane. The unit in all axes is µm.

7.3 Image filtering, registration and volume rendering

Prior to the image registration, a pre-treatment of the 3D tomography data to remove the artefacts was required. As shown on the 2D slice (XY-plane) in Fig. 3b, there are many bright horizontal lines, which cross the crack region. Those bright horizontal lines on the 2D slices are actually horizontal planes on XY-planes when observed on 3D volume rendering, as shown in Fig. 3a. Due to the large width (25mm) of the specimen, X-rays are fully absorbed for a range of angles as the thick direction aligns with the beam direction. Consequently, reconstruction of the tomographic data results in artefacts that appear as bright horizontal lines (cross-hatched shading in Fig. 3b). A filter module based on fast Fourier transform algorithm is used to remove these artefacts on the 2D slices. Fig. 22c shows the slice after performing filtering to the slice shown in Fig. 22b. After removing artefacts on the reconstructed 3D tomography datasets, overlapping sample volumes (layer-1 and layer-2) are matched based on image registration. Image registration procedure is based on feature detection, feature matching, mapping function design, and image transformation and resampling [43]. Crack features are used to align the two volume elements to reconstruct the entire crack geometry.

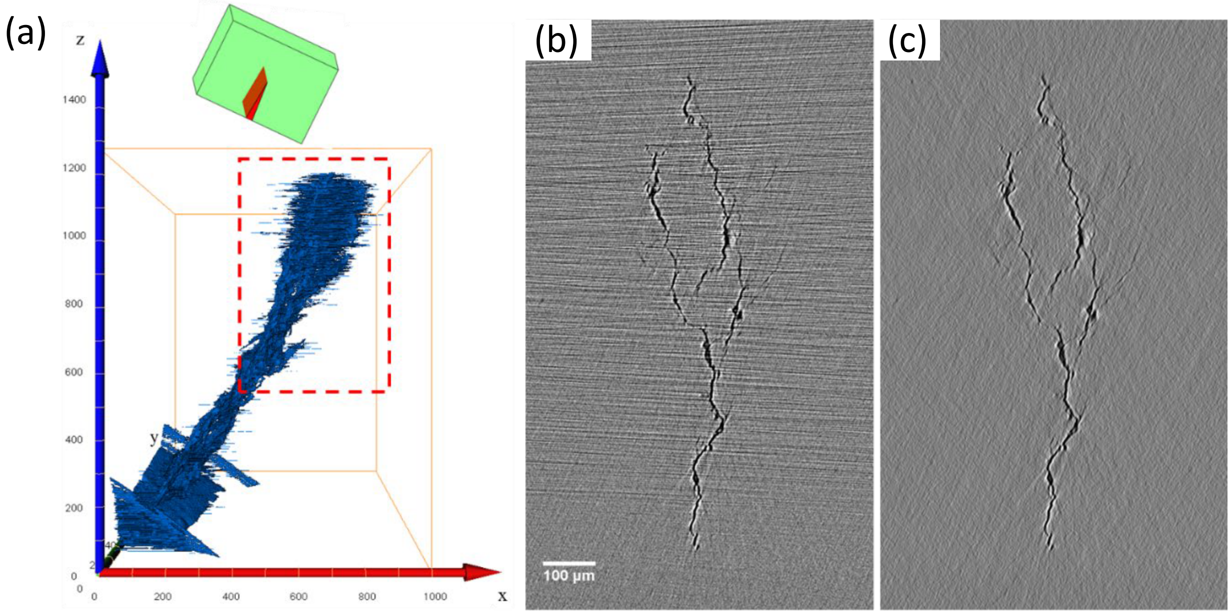

Fig. 22. 3D image filtering. (a) 3D volume rendering of the crack (layer-1) before image filtering. The red dash rectangle indicates the region with artefacts. (b) Ortho slice (slice 1020 in XY-plane) before filtering, and (c) the same slice obtained by Fourier transform filtering to remove stripes (artefacts) in the horizontal direction in B.

Visualizing the crack is achieved by thresholding the linear absorption coefficient (LAC) for each voxel [44]. Accurately extracting the whole crack volume however depends on the choice of threshold in the 16-bit grayscale image; the threshold value selected will determine the interface position between the crack and the matrix [45]. For this investigation, an intermediate value was taken corresponding to the valley between the air and steel absorption peaks in the 16-bit LAC distribution. Finally, a 'seed' growth technique for voxel continuity was applied to eliminate noise, to create a fully connected 3D voxel set representing the crack and interface. Those voxels that belong to the crack are set at fully opaque, whereas the voxels belonging to the matrix are set at fully transparent.

7.4 3D Visualization and Analysis of the Crack

The full 3D crack reconstruction yields a 3D volume (Fig. 23) rendering of the crack with multiple crack branches. The volume rendering of the crack was aligned to be parallel to the YZ-plane. The main crack volume is labelled with blue colour. Crack branches are labelled with different colours in order to differentiate them from the main crack. The extracted crack volume is projected onto YZ-plane for both positive X (Fig. 23b) and negative X (Fig. 23d) direction, which is perpendicular to the loading direction. Optical image (Fig. 23c) is used to compare the surface crack with the 3D crack morphology. The corrosion pits (1-2) and crack jumps (3-4) are matched between optical surface observation (Fig. 23c) and 3D tomography results (Fig. 23B-D). (1) and (5) indicates the edge of the crack appears on the sample surface.

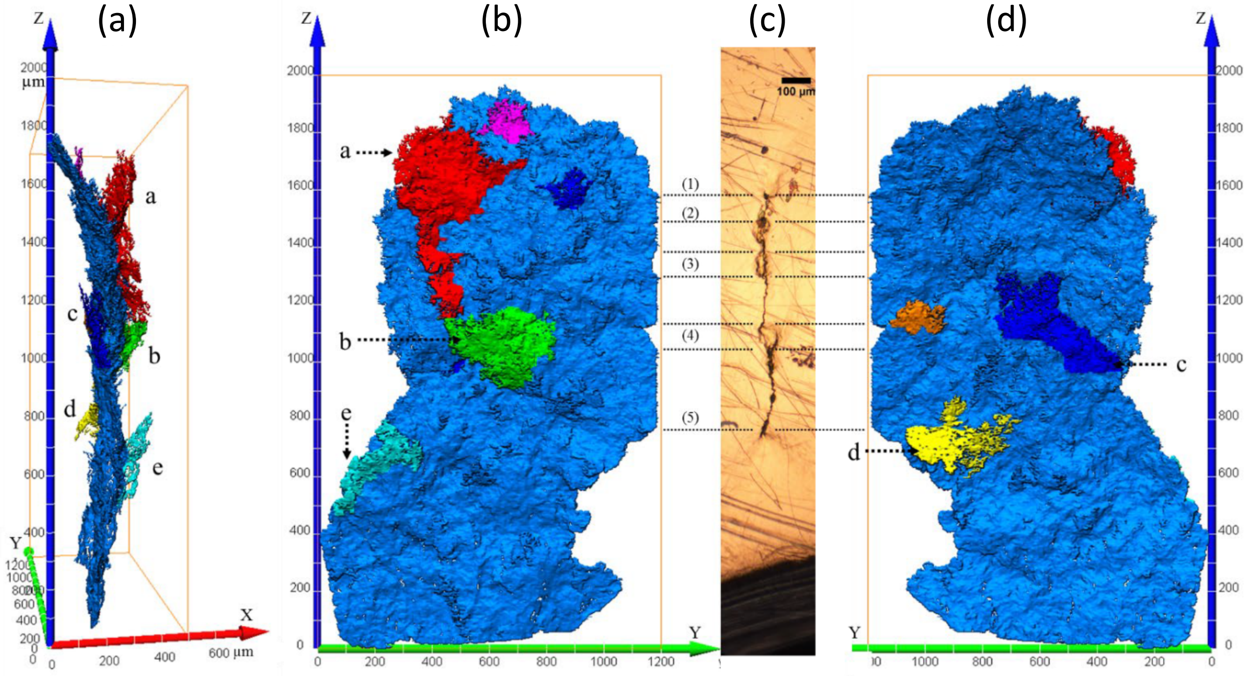

Fig. 23. (a) 3D volume rendering of the crack with multiple crack branches. A projection of the crack volume onto YZ-plane on (b) positive X direction and (d) negative X direction. a - e indicate five different crack branches labelled with different colours. The unit in each axis is µm. (c) Microscope image showing the morphology of the crack on the sample surface. (1) and (2) show pits on the sample surface, (3) and (4) show crack jumps, (5) indicates the edge of the surface crack.

To observe the crack branches in more details, 2D ortho-slices with progressively increasing depth for crack branch-a and -c were carefully selected and extracted from the 3D volume. Fig. 24A shows a selected crack volume from 1100 to 2000 in Z-axis to show the branch-a (red). Figs. 24(a)-(e) show 2D slices from slice 320 to slice 560 on XZ-plane (see Fig. 23), with interval of 60 slices (60µm). The data volume from 1100 to 2000 is cropped to show the crack branch-a. The white solid arrow and black arrow indicate the upper and lower parts of the crack branch-a in Fig. 23, and the white dash arrow is a part of the main crack.

Crack branch-a is also observed on XY-plane. Fig. 25(a)-(e) are 2D slices from slice 1480 to slice 1800 (XY-plane), with interval of 80 slices (80µm). The white solid arrow indicates the crack branch-a in Fig. 23.

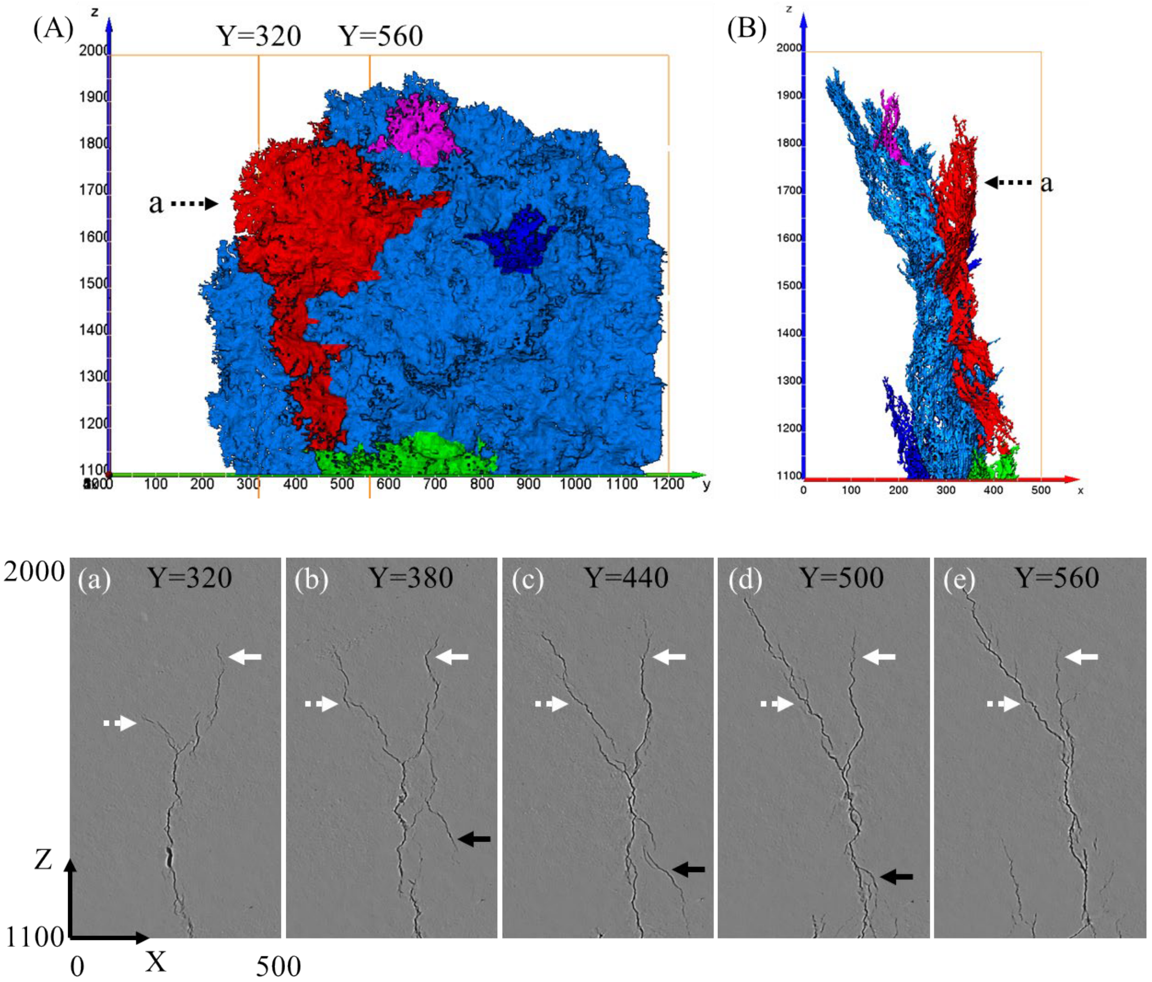

Fig. 24. Projection of the crack onto (A) YZ-plane and (B) XZ-plane to show the branch-A (red), with a range of 1100-2000 in Z-axis. (a)-(e) are 2D slices from slice 320 to slice 560 on XZ-plane, with interval of 60 slices (60μm). The white solid arrow and black arrow indicate the upper and lower parts of the crack branch-a, and the white dash arrow is a part of the main crack. The unit in each axis is μm.

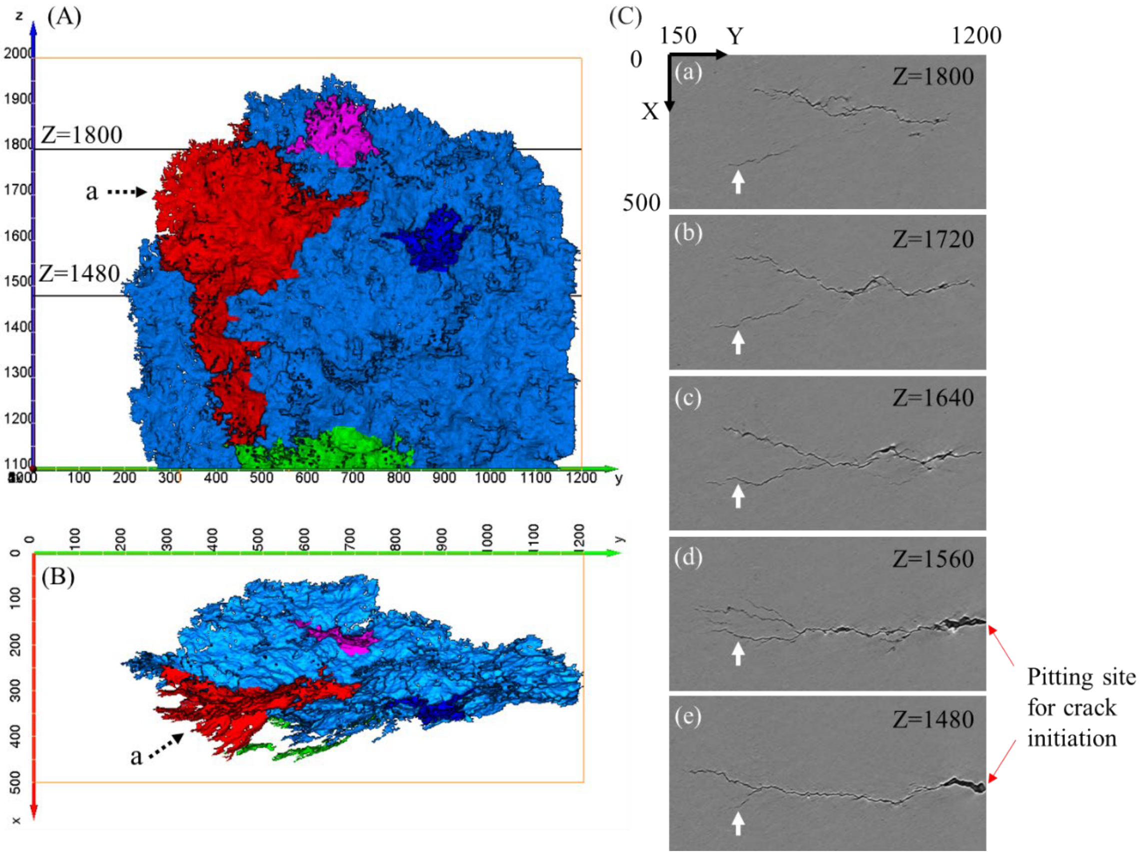

Fig. 25. Projection of the crack onto (A) YZ-plane and (B) XY-plane to show the branch-a (red), with a range of 1100-2000 in Z-axis. (a)-(e) are 2D slices from slice 1480 to slice 1800 on XY-plane, with interval of 80 slices (80μm). The white solid arrow indicates the crack branch-a. The unit in each axis is μm.

2D ortho-slices of crack branches-b and -c with progressively increasing depth are also carefully selected and extracted from the 3D volume. Fig. 26A shows a selected crack volume from 800 to 1400 in Z-axis to show the branch-c (green) and branch-c (blue). Fig. 26(a)-(e) show 2D slices from slice 520 to slice 760 on XZ-plane, with interval of 60 slices (60μm). Fig. 27(a)-(e) are 2D slices from slice 960 to slice 1280 on XY-plane, with interval of 80 slices (80μm). The dash arrow and solid arrow indicate the crack branch-b and -c, respectively. Fig. 26(a) is a slice (Y=520, XZ-plane) near the edge of crack branch-b and -c, where two small branches are formed near the main crack. As the slice depth increase from 520 (a) to 640 (c), the length of crack branches increase and the branches reach deep into the matrix. The section of the main crack between branch-b and

-c start to diminish after slice depth 640 (c) and disappear in (d), where the branch-b become a part of the main branch.

From 2D ortho-slices on XY-plane as shown in Fig. 26(a)-(e), the branch-c (white solid arrow) formed a new sub-branch in (b) and start to diminish in (e). The edge of branch-b (white dash arrow) is shown in (a) as a single branch, but three sub-branches are formed in (c). Those three sub-branches converged into a main crack with small branches reach into the matrix, as shown in Fig. 26(d) and (e).

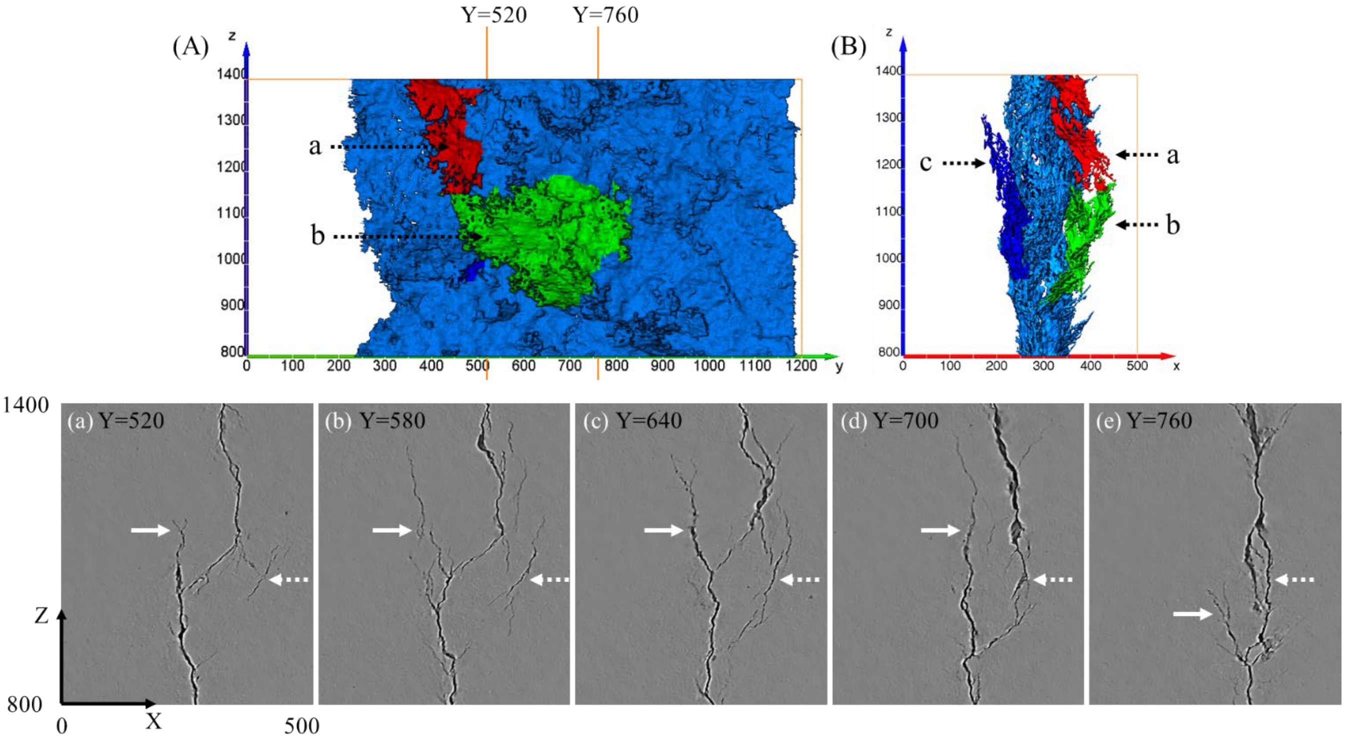

Fig. 26. Projection of the crack onto (A) YZ-plane and (B) XZ-plane to show the branch-b (green) and branch-c (blue), with a range of 800 - 1400 in Z-axis. (a)-(e) are 2D slices from slice 520 to slice 760 on XZ-plane, with interval of 60 slices (60μm). The dash arrow and solid arrow indicate the crack branch-b and -c, respectively. The unit in each axis is μm.

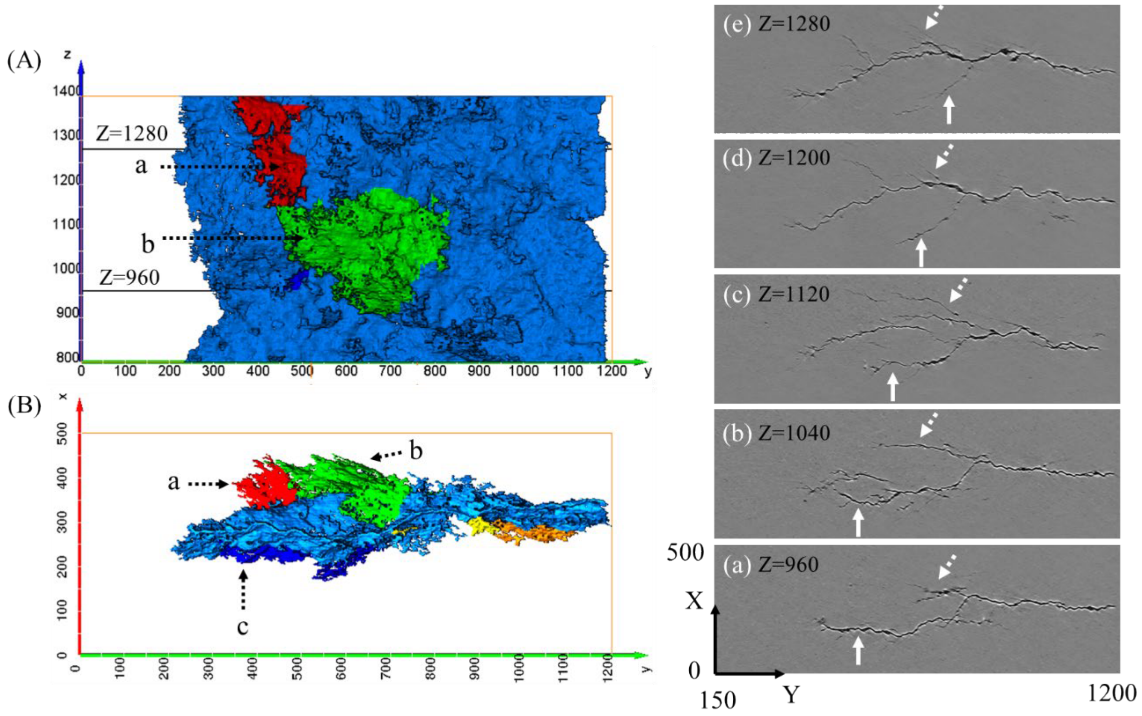

Fig. 27. Projection of the crack onto (A) YZ-plane and (B) XY-plane to show the branch-b (green) and branch-c (blue), with a range of 960 - 1280 in Z-axis. (a)-(e) are 2D slices from slice 960 to slice 1280 on XY-plane, with interval of 80 slices (80μm). The dash arrow and solid arrow indicate the crack branch-b and -c, respectively. The unit in each axis is μm.

8. Conclusion

In this paper, we reported the finding of an extensive NDT program conducted on a small sample of stainless steel with two cracks of mm-scale sizes. This is a preliminary study aimed at evaluating the capabilities of several NDT tools that could eventually be deployed in the field to image SCC in stainless steel canisters. There is a tradeoff between the ease of implementation (and applicability in the field) and level of detail that can be obtained from the technique. For instance, a detailed 3D image of the crack could be obtained with X-ray tomography, but this technique cannot be deployed in the field. On the other hand, NRUS was shown to be a powerful and easy to implement tool for detecting the presence of one or multiple cracks but cannot be used to locate or image the cracks. Ultrasonic C-scans could image the cracks and their penetration depth. However, the probe needs to be coupled to the structure with a fluid, which would require some engineering design if this technique were to be deployed inside the concrete overpack. More importantly, C-scans cannot differentiate a cracks from a notch or surface scratch because of the physics involved in the imaging processing (echoing of the incident ultrasonic waves). Vibrothermography and LEGIT provide very similar images of the cracks and are transparent to the presence of surface scratches. These two techniques are based on the same physical mechanism, namely, the clapping (opening and closing) of the cracks interacting with the incident ultrasonic waves. Vibrothermography exploits temperature changes whereas LEGIT exploits the generation of harmonics by the cracks for detection and wave-field discontinuities at the crack for imaging. Vibrothermography cannot be currently deployed in the field because of the geometrical constraints in the concrete overpack. The infrared camera would have to be miniaturized and shielded from the radiations for the technology to be deployable. However, LEGIT could be deployed with some changes to the setup and equipment. The large scanning laser head used in our experiments could be replaced by a fiber-optic sensor head (e.g., the OFV-55x device from Polytec). Such a device does not have built-in scanning capabilities but could be moved and operated by a dedicated robot to scan the surface. The transducer glued to the surface in our experiment could be replaced by a non-contact EMAT transducer, which was already accomplished elsewhere [5,6]. The engineering of such technologies is beyond the scope of this study. Future work could include a similar study on much larger samples, as an intermediate step between the current study and the field application.

Acknowledgements

This work was funded by the U.S. Department of Energy, Nuclear Energy University Program through Integrated Research Project Award Number DE-NE0008442.

References

1. R. M. Kain, “Marine Atmospheric Stress Corrosion Cracking of Austenitic Stainless Steels,” Materials Performance, 29(12), pp. 60-62 (1990).

2. EPRI 2014, “EPRI Flaw Growth and Flaw Tolerance Assessment for Dry Cask Storage Canisters,” Presentation to the NRC, August 5, 2014, EPRI, Palo Alto, CA.
3. C. Bryan and D. Enos, “Analysis of Dust Samples Collected from Spent Nuclear Fuel Interim Storage Containers at Hope Creek, Delaware, and Diablo Canyon, California,” SAND2014-16383, Sandia National Laboratories, Albuquerque, NM, (2014).
4. R. M. Meyer, A. F. Pardini, J. M. Cuta, H. E. Adkins, A. M. Casella, H. Qiao, M. R. Larche, A. A. Diaz, S. R. Doctor, “NDE to Manage Atmospheric SCC in Canisters for Dry Storage of Spent Fuel: an Assessment,” PNNL-22495, Pacific Northwest National Lab Laboratory, Richland, WA (2013).
5. C. J. Lissenden, S. Choi, H. Cho, A. Motta, K. Hartig, X. Xiao, S. Le Berre, S. Brennan, K. Reichard, R. Leary, B. McNelly, I. Jovanovic, “Toward robotic inspection for dry storage casks for spent nuclear fuel,” J. Pressure Vessel Technol., **139**(3), pp. 031602 (2017).
6. S. Choi, H. Cho, C. J. Lissenden, “Nondestructive Inspection of Spent Nuclear Fuel Storage Canisters Using Shear Horizontal Guided Waves,” Nuclear Engineering and Technology, **50**(6), pp. 890-898 (2018).
7. J. Blitz and G. Simpson, Ultrasonic Methods of Non-Destructive Testing (London, Springer, 1996).
8. L. W. Schmerr, Fundamentals of Ultrasonic Nondestructive Evaluation (Plenum, New York, 1998).
9. P. A. Johnson, B. Zinszner, and P. N. J. Rasolofosaon, “Resonance and elastic nonlinear phenomena in rock,” J. Geophys. Res. 101(B5), 11553 (1996).
10. J. A. TenCate, D. Pasqualini, S. Habib, K. Heitmann, D. Higdon, and P. A. Johnson, “Nonlinear and Nonequilibrium Dynamics in Geomaterials,” Physical Review Letters, 93(6), 065501 (2004).
11. K. L. Reifsnider, E. G. Henneke, and W. W. Stinchcomb, “The Mechanics of Vibrothermography.” In: W. W. Stinchcomb, editor. Mechanics of Nondestructive Testing, New York: Plenum; 1980, p. 249-276.
12. J. Renshaw, J. C. Chen, S. D. Holland, and R. B. Thompson, “The sources of heat generation in vibrothermography,” NDT&E International, 44(8), pp. 736-739 (2011).
13. S. S. Singh, J. J. Williams, M. F. Lin, X. Xiao, F. De Carlo, and N. Chawla, “In situ investigation of high humidity stress corrosion cracking of 7075 aluminum alloy by three-

dimensional (3D) X-ray synchrotron tomography," Materials Research Letters, 2(4) pp. 217-220 (2014).

14. X. Shan, and J. H. Payer, "Comparison of Ceramic and Polymer Crevice Formers on the Crevice Corrosion Behavior of Ni-Cr-Mo Alloy C-22". In CORROSION 2007, NACE International.
15. X. Shan, H. Ha, and J. H. Payer, "Comparison of Crevice Corrosion of Fe-Based Amorphous Metal and Crystalline Ni-Cr-Mo Alloy," Metallurgical and Materials Transactions a-Physical Metallurgy and Materials Science, 40a(6): pp. 1324-1333 (2009).
16. X. Shan, and J. H. Payer, "Effect of Polymer and Ceramic Crevice Formers on the Crevice Corrosion of Ni-Cr-Mo Alloy 22," Corrosion, **66**(10), pp. 105005 (2010).
17. D. E. Bray, and R. K. Stanley, Nondestructive Evaluation: A tool in Design, Manufacturing and Service (Boca Raton, CRC Press, 1997)
18. L. W. Kesseler, "Review of Progress and Applications in Acoustic Microscopy," Journal of the Acoustical Society of America, 55(5), pp. 909-918 (1974).
19. C. F. Quate, A. Atalar, H. K. Wickramasinghe, "Acoustic Microscopy with Mechanical Scanning - A Review," Proceeding of the IEEE, 67(8) pp. 1092-1114 (1979).
20. T. M. Moore, "C-Mode Acoustic Microscopy Applied to Integrated Circuit Package Inspection," Solid-State Electronics, 35(3), pp. 411-421 (1992).
21. A. Todoroki, and H. Kobayashi, "Image Analysis of Delamination Cracks in Carbon-Fibre Composites by Scanning Acoustic Microscopy," Composites Science and Technology, 52(4), pp. 551-559 (1994).
22. A. Briggs, Advances in Acoustic Microscopy (Plenum Press, New York, 1995).
23. R. G. Maev, Acoustic Microscopy: Fundamentals and Applications (Wiley-VCH, Weinheim, 2008).
24. Y. Zheng, R. G. Maev, and I. Y. Solodov, "Nonlinear Acoustic Applications for Material Characterization: A Review," *Canadian Journal of Physics,* **77**(12), pp. 927-967 (2000).
25. P. Nagy, "Fatigue Damage Assessment by Nonlinear Ultrasonic Materials Characterization," Ultrasonics 36(1-5), pp. 375-381 (1998).
26. P. A. Johnson, "The New Wave in Acoustic Testing," Mat. World **7**, 544-546 (1999).

27. D. Pasqualini, K. Heitmann, J. A. TenCate, S. Habib, D. Higdon, and P. A. Johnson, Nonequilibrium and Nonlinear Dynamics in Berea and Fontainebleau Sandstones: Low-Strain Regime," Journal of Geophysical Research, 112, B01204 (2007).
28. K. Van Den Abeele, P. Y. Le Bas, B. Van Damme, and T. Katkowski, "Quantification of Material Nonlinearity in Relation to Microdamage Density Using Nonlinear Reverberation Spectroscopy: Experimental and Theoretical Study," Journal of the Acoustical Society of America, 126(3), pp. 963-972 (2009).
29. S. M. Hogg, B. E. Anderson, P.-Y. Le Bas, and M. C. Remillieux, "Nonlinear resonant ultrasound spectroscopy of stress corrosion cracking in stainless steel rods," NDT&E International 102, pp. 194-198 (2019).
30. K. V. D. Abeele, "Multi-mode nonlinear resonance ultrasound spectroscopy for defect imaging: An analytical approach for the one-dimensional case," Journal of the Acoustical Society of America, 122(1), 73-90 (2007).
31. Y. Ohara, B. E. Anderson, T. J. Ulrich, P.-Y. Le Bas, P. A. Johnson, and S. Haupert, "Localization of closed cracks using multi-mode nonlinear resonant ultrasound spectroscopy," Journal of the Japanese Society for Non-Destructive Inspection, 64, pp. 571-578 (2015).
32. L. D. Favro, R. L. Thomas, X. Han, Z. Ouyang, G. Newaz, and D. Gentile, "Sonic Infrared Imaging of Fatigue Cracks," International Journal of Fatigue, 23, pp. S471-S476 (2001).
33. C. Gao, W. Q. Meeker, and D. Mayton, "Detecting Cracks in Aircraft Engine Fan Blades Using Vibrothermography Nondestructive Evaluation," Reliability Engineering & System Safety, 131, pp. 229-235 (2014).
34. F. Mabrouki, M. Thomas, M. Genest, and A. Fahr, "Frictional Heating Model for Efficient Use of Vibrothermography," NDT&E International, 42, pp. 345-352 (2009).
35. J. Renshaw, S. D. Holland, R. B. Thompson, and C. Uhl, "The Effect of Crack Closure on Heat Generation in Vibrothermography. In: D. O. Thompson, D. E. Chimenti, editors. Review of progress in quantitative nondestructive evaluation, vol. 28A, pp. 473-480 (2009).
36. W. Phil, W., An Introduction to Synchrotron Radiation: Techniques and Applications. 2011: Chichester, West Sussex, U.K.: Wiley, (2011).

37. P. J. Withers, “Fracture Mechanics by Three-Dimensional Crack-Tip Synchrotron X-ray Microscopy,” Philosophical Transactions of the Royal Society A: Mathematical, Physical and Engineering Sciences, 373(2036): pp. 20130157 (2015).
38. N. T. Vo, R. C. Atwood, and M. Drakopoulos, “Superior Techniques for Eliminating Ring Artifacts in X-ray Micro-Tomography,” Optics Express, 26(22), pp. 28396-28412 (2018).
39. S. S. Singh, T. J. Stannard, X. Xiao, and N. Chawla, “In Situ X-ray Microtomography of Stress Corrosion Cracking and Corrosion Fatigue in Aluminum Alloys,” JOM, 69(8), pp. 1404-1414 (2017).
40. S. C. Wu, T. Q. Xiao, and P. J. Withers, “The Imaging of Failure in Structural Materials by Synchrotron Radiation X-ray Microtomography,” Engineering Fracture Mechanics, 182, pp. 127-156 (2017).
41. J. Y. Buffiere, E. Ferrie, H. Proudhon, and W. Ludwig, “Three-Dimensional Visualisation of Fatigue Cracks in Metals Using High Resolution Synchrotron X-ray Micro-Tomography,” Materials Science and Technology, 22(9), pp. 1019-1024 (2006).
42. J.-Y. Buffiere, E. Maire, J. Adrien, J.-P. Masse, and E. Boller, “In Situ Experiments with X ray Tomography: an Attractive Tool for Experimental Mechanics,” Experimental Mechanics, 50(3), pp. 289-305 (2010).
43. B. Zitova and J. Flusser, “Image Registration Methods: A Survey.” Image and Vision Computing, **21**(11), pp. 977-1000 (2003).
44. H. Zhang, H. Toda, P. C. Qu, Y. Sakaguchi, M. Kobayashi, K. Uesugi, and Y. Suzuki, “Three-Dimensional Fatigue Crack Growth Behavior in an Aluminum Alloy Investigated with In Situ High-Resolution Synchrotron X-ray Microtomography,” Acta Materialia, **57**(11), pp. 3287-3300 (2009).
45. H. Toda, S. Yamamoto, M. Kobayashi, K. Uesugi, and H. Zhang, “Direct measurement procedure for three-dimensional local crack driving force using synchrotron X-ray microtomography,” Acta Materialia, **56**(20), pp. 6027-6039 (2008).